

**DESIGN AND OPTIMIZATION OF A VORTEX PARTICLE SEPARATOR FOR
A HOT MIX ASPHALT PLANT USING COMPUTATIONAL FLUID
DYNAMICS**

A Thesis
Presented to
The Academic Faculty

By

Andrew M. Hobbs

In Partial Fulfillment of the
Requirements for the Degree of
Masters of Science in the
School of Mechanical Engineering

Georgia Institute of Technology
December 4, 2002

**Design and Optimization of a Vortex Particle Separator for a Hot Mix Asphalt
Plant Using Computational Fluid Dynamics**

Approved:

Marc K. Smith, Chairman

S. Mostafa Ghiaasiaan

Sam V. Shelton

Date Approved 8/12/03

TABLE OF CONTENTS

	Page No.
LIST OF TABLES	v
LIST OF FIGURES	vi
ABBREVIATIONS	viii
NOMENCLATURE	ix
SUMMARY	x
CHAPTERS	
I. INTRODUCTION	1
II. PROCEDURE	10
Turbulence Model	12
Simulation Parameters	18
Particle Tracking	19
Horizontal Cyclone	23
III. RESULTS AND DISCUSSION	25
Blade Geometry	25
Flow Results	28
Grid Study	32
Separation Distance	34
Annular Gap Distance	35
Axial Gap Distance	41
Discrete Phase Modification	42
Horizontal Cyclone Results	45
IV. CONCLUSION	51
APPENDIX A	54
APPENDIX B	55
APPENDIX C	56
APPENDIX D	58

APPENDIX E	60
APPENDIX F	62
BIBLIOGRAPHY	63

LIST OF TABLES

Table No.	Description	Page No.
1	Results of collection efficiency as a function of cell count	34
2	Results of DRW and mean velocity particle tracking	43
3	Results of incomplete particles for 10,000 and 20,000 steps for 125 μm particle	48
4	Particle tracking data for 10,000 steps	48

LIST OF FIGURES

Figure No.	Description	Page No.
1	HMA plant component schematic showing material and gas flows	2
2	Reverse flow cyclone showing dirty gas stream inlet and clean gas outlet	4
3	Horizontal cyclone design showing inlet, outlet, and collection hopper	5
4	Key components and variables of inline vortex separator	7
5	Vortex separator showing key variables and vortex tube (blue)	12
6	Front elevation of blade and hub geometry showing sweep angle	25
7	Side elevation of blade and hub geometry showing departure angle	26
8	Sweep blade angle versus pressure drop for departure angles 45, 50, and 60°	27
9	Sweep angle versus tangential velocity for departures angles 45, 50, and 60°	27
10	Contours of tangential velocity on the midplane	29
11	Contours of axial velocity on the midplane	29
12	Contours of static pressure in inches of water column on the midplane and blades	30
13	Pathlines release from the inlet colored by velocity magnitude	30
14	Single injection trajectory tracks for 150 and 75 micron diameter particles	31
15	Collection efficiency as a function of cell count	33
16	Collection efficiency as a function of separation distance	35
17	Particle efficiency as a function of annular gap distance	36

18	Device showing flange section (in green) next to collection box	36
19	Side elevation detail of flange section showing annular gap	37
20	Effect of flange section on collection efficiency	38
21	Contours of axial velocity on midplane for non-flanged geometry	39
22	Contours of axial velocity on midplane for flanged geometry	39
23	Contours of static pressure on the midplane for non-flanged geometry	40
24	Contours of static pressure on the midplane for the flanged geometry	40
25	Side elevation showing axial gap detail	41
26	Collection efficiency as a function of axial gap distance	42
27	Final design collection efficiency showing DRW model and mean velocity	43
28	Collection efficiency for varied coefficient of restitution	44
29	Horizontal cyclone showing pathlines released from the inlet	46
30	Horizontal cyclone showing contours for tangential velocity	46
31	Horizontal Cyclone showing contours of static pressure	47
32	Predicted collection efficiency and experimental data for horizontal cyclone	49
33	Predicted efficiencies for vortex separator and horizontal cyclone	50

ABBREVIATIONS

HMA	hot mix asphalt
CFD	computational fluid dynamics
DNS	direct numerical simulation
RANS	Reynolds Average Navier-Stokes
RSM	Reynolds stress model
RNG	Renormalization group
DPM	Discrete Phase Model
DRW	Discrete Random Walk
CoR	coefficient of restitution

NOMENCLATURE

a	speed of sound	$C_{2\epsilon}$	RNG constant
Re_t	turbulent Reynolds number	β	RNG constant
Re_p	particle Reynolds number	η_0	RNG constant
u_i	total velocity	y^*	wall unit
\bar{u}_i	mean velocity	U^*	mean velocity from wall
u'_i	fluctuating velocity	U_p	mean velocity
ρ	fluid density	y_p	distance to the wall
p	pressure	τ_w	wall shear stress
g	gravity	k_p	turbulent kinetic energy
τ_{ij}	stress tensor	κ	constant in wall formulation
δ_{ij}	Kronecker delta	E	constant in wall formulation
μ	molecular viscosity	ν	kinematic viscosity
k	turbulent kinetic energy	η	Kolmogorov length scale
ϵ	turbulent dissipation rate	f_{drag}	drag force
μ_t	turbulent viscosity	u_p	particle velocity
μ_{eff}	RNG effective viscosity	ρ_p	particle density
S	RNG formulation term	d_p	particle diameter
μ_{t0}	turbulent viscosity w/o swirl	C_D	drag coefficient
α_s	swirl constant	s	particle surface area
Ω	characteristic swirl number	ϕ	shape factor
C_μ	RNG constant	S_s	area of same volume sphere
α_k	RNG constant		
$C_{1\epsilon}$	RNG constant		

SUMMARY

The intent of this study was to optimize an inline cyclonic type separator to meet the unique performance requirements of a hot mix asphalt plant using computational fluid dynamics (CFD) methods. The design goals were to develop a device which would collect the maximum percent of particles greater than 150 μm in diameter and the minimum percentage of particle smaller than 150 μm at a minimum pressure drop. Flow solutions were solved using the commercial CFD code Fluent based on a nominal flowrate and operational conditions. Once a converged solution was obtained, particle tracking studies were performed to determine the collection efficiency of the design. Key dimensions were varied to investigate the effects on collection efficiency.

In addition, the existing horizontal cyclone separator was modeled and flow simulations were performed. Particle tracking studies were used to calculate collection efficiency and the results were compared to experimental data. The CFD results were shown closely reflect the experimental data for pressure drop and collection efficiency. The final design iteration vortex separator was shown to surpass the performance of the existing horizontal cyclone design. Modifications were made to the particle tracking model including non-spherical drag model and the coefficient of restitution to better simulate irregular shaped dust particles. The proposed design was shown to meet the performance requirements for a range of particle characteristics.

CHAPTER I

INTRODUCTION

Roads have been a fundamental part of civilized infrastructure for cultures dating back to the Egyptians in 3000 BC. The Roman highway called the Appian Way, built in 244 BC, was made of polygonal top stones and lava. This surface was called *pavimentum* from which we derive the modern term *pavement*. Over time, road construction methods and materials have changed. The road surface which we know today as pavement is properly called hot mix asphalt.

Hot mix asphalt (HMA) is the most common road surfacing material used in the United States. Between 450,000,000 and 500,000,000 tons of hot mix asphalt are produced annually in the U.S. alone. HMA is comprised of sand and various sizes of crushed rock, called aggregate, which is mixed together with liquid asphalt cement. The liquid asphalt cement acts as a binder. The mixture is thermoformable and begins to set at temperatures below 300° F.

The modern hot mix asphalt plant is comprised of several components, each of which performs a specific task in the production of the asphalt mixture. Figure 1 illustrates the process. Aggregate is typically stored in large stockpiles outdoors where it is exposed to the weather. Any moisture in the aggregate can cause poor coating so the aggregate must be dried before the liquid asphalt can be introduced. The aggregate is loaded into feeder bins which meter out the different sized aggregate. The aggregate is then fed into a rotating drum where it is tumbled while being exposed to hot gases from a burner. Once the aggregate is dry, it is mixed with the liquid asphalt cement and stored in an insulated silo until it is loaded into trucks to be taken to the jobsite.

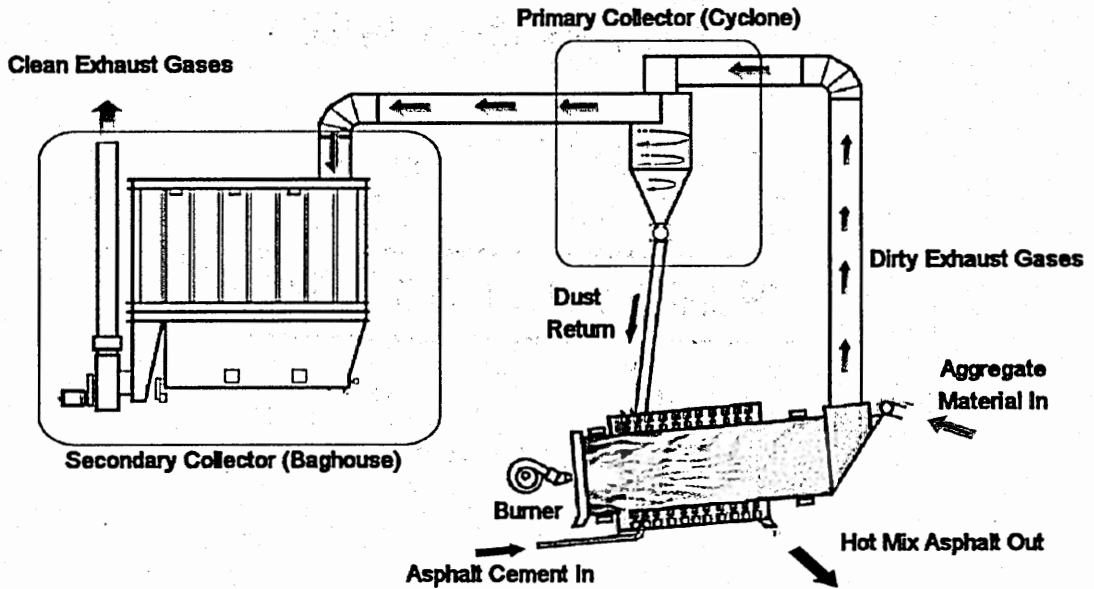


Figure 1. HMA plant component schematic showing material and gas flows

As aggregate is dried in the drum by the hot gases from the burner, dust from the aggregate is carried away in the exhaust gases. Particulate in the exhaust gas stream must be removed to meet current environmental emission standards, making the separation of particulate from the exhaust gases a necessary step in the production of hot mix asphalt. In addition, HMA mix design requires a certain percentage of fine material or *finer* to be included in the mix. The fine material to be included in the mix is made up of dust and sand larger than 150 μm . A certain quantity of this sized material is needed to give the asphalt mix the desired properties. Any of this fine material entrained in the gas stream must be separated and returned to the mix.

Cleaning and separating is traditionally accomplished in two stages: an inertially driven primary collector and a fabric filter-based secondary collector. Nominally, the primary collector removes all particles larger than approximately 150 μm and passes all

particles smaller than 150 μm to the secondary collector (J.D. Brock, 1999). The larger particles are added to the HMA mix and the smaller particles remain in the gas stream. Traditionally, a cyclone is used as the primary collector.

The secondary collector is typically a fabric filtration system called a baghouse. Particulate accumulates on the fabric media forming a thin layer of dust called a "cake." It is the cake which actually accomplishes the filtration of the smallest particles. Large particles make the cake more porous allowing smaller particles to pass through unfiltered. Large particles can also cause abrasion, leading to shortened bag life. Hence it is necessary for the primary collector to remove the larger particles but pass the smaller particles (M. Swanson, 1999).

The limiting factor of the filtration system is the fan horsepower required to pull air through the pre-collector and the filter media. Because of this, minimizing the pressure drop associated with the overall filtration process is a key design consideration. However, most cyclones are typically designed for maximum efficiency with less concern for pressure drop. The design requirements of the primary collector in a HMA plant are unique. It must be able to remove large particles (greater than 100 μm) very efficiently while passing the majority of the small particles at a relatively low pressure drop for a nominal flow rate of 67,000 ft^3/min .

The traditional reverse flow cyclone design is comprised of a vertical cylinder with a conic section at the bottom as illustrated in Figure 2. Flow is introduced tangentially toward the top of the cylinder and leaves via a tube called the vortex tube which extends down the center of the cylinder. The tangential inlet creates a swirling flow about the axis of the main cylinder body. Inertial forces move the swirling particles

with more mass toward the wall. Once they reach the wall, gravity pulls them down, and they are collected. Particles which do not have enough mass or density are pulled toward

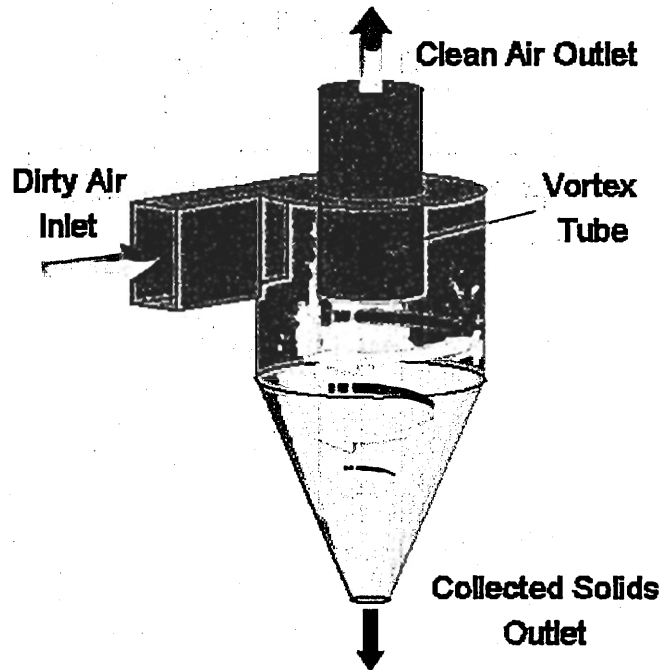


Figure 2. Reverse flow cyclone showing dirty gas stream inlet and clean gas outlet

the central low pressure region and exit the cyclone thru the vortex tube. Depending on the mass and density of the particles, some particles will be collected, and some particles will escape via the vortex tube. The size at which 50% of the particles are collected and 50% are passed is called the 50% cut size.

Cyclonic separators are a common method of particle removal because they have no moving parts and can withstand high operational temperatures with relatively inexpensive maintenance costs. However, due to the unique combination of conditions and the performance requirements of a HMA plant, a traditional reverse flow cyclone is

not optimally suited as a primary collector. The high flow rates and relatively large cut size require such a cyclone to be quite large. In addition the pressure drop for such a device places a large drain on the available power of the system fan.

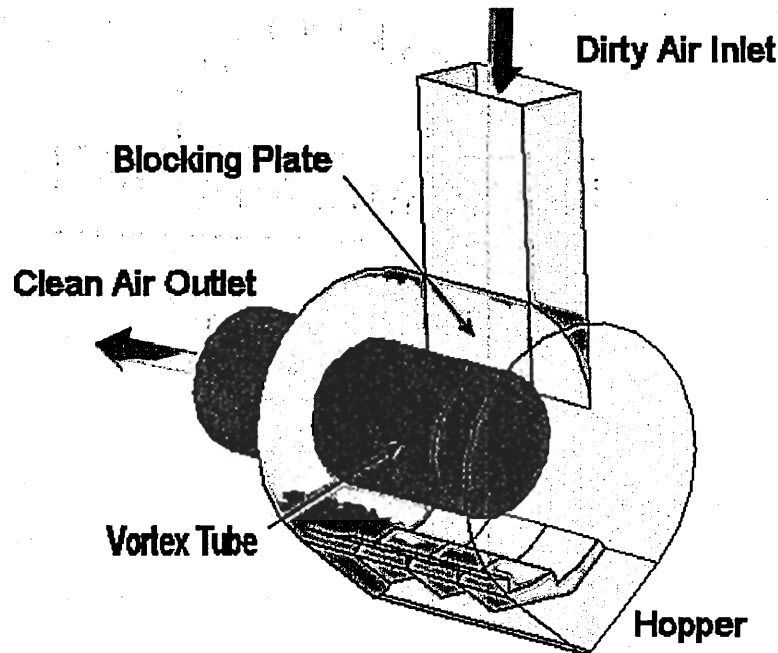


Figure 3. Horizontal cyclone design showing inlet, outlet, vortex tube, blocking plate, and collection hopper

Astec Industries introduced a variation of the reverse flow cyclone in which the tangential inlet is vertical and the axis of fluid rotation and the vortex tube are horizontal. Figure 3 shows this design. The horizontal cyclone currently in use by Astec Industries in their asphalt plants differs from a reverse flow cyclone in its orientation and in other more subtle ways. A metal blocking plate extends from the inlet to the vortex tube which blocks off swirling flow from circling the vortex tube in the inlet region. This

modification lowers the pressure drop by limiting the swirling in the inlet region. Instead of being perfectly cylindrical, the horizontal cyclone has a sloped hopper which collects dust separated from the flow. Three skimmer plates are positioned over this hopper. The skimmer plates shield the hopper from high velocity flow. The nominal pressure drop across this device during operational conditions is 3 inches of water (747 Pa). The horizontal cyclone affords adequate efficiencies and a lower pressure drop than a comparably sized reverse flow cyclone.

Cyclone technology is over a hundred years old, and while the precise nature of the flow within the cyclone is not fully known, there has been much empirical and theoretical study which has provided a general understanding of characteristic performance. Much of the development in cyclone design has come as a result of trial and error experimentation. While this type of experimentation yields the most accurate results, it is time consuming and costly. Empirical and semi-empirical models of cyclone behavior have been developed, but their usefulness is often very limited if the geometry does not sufficiently match the model. The use of computational fluid dynamics (CFD) software to predict the performance of a cyclone has been shown to be more accurate than empirical models, and the analysis can be performed in shorter time and with less cost than physical experimentation (Griffiths and Boysan, 1996; Ma *et al.*, 2000).

The cyclone design which is the subject of this paper is an inline vortex separator. Inline cyclonic separators have been studied as early as the late 1950's by Daniels (1957). This design is comprised of a fixed set of stationary vanes placed in a circular duct of a set diameter as shown in Figure 4. The main duct continues from the guide vanes until a second circular duct of a smaller diameter (analogous to and hence

called the vortex tube) joins it forming an annular slit. A collection box encompasses the annular slit. The design uses the stationary vanes to generate a swirling airflow. The centrifugal force on the particles in the flow causes them to move radially outward. At the point where the smaller diameter duct creates the annular slit, particles either pass out the smaller outlet tube or they pass through the annular slit and are collected in the collection box.

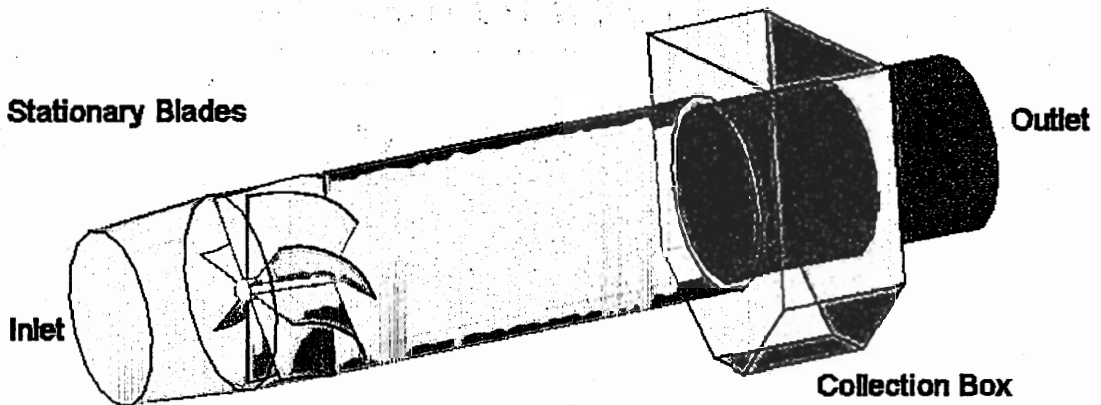


Figure 4. Key components and variables of inline vortex separator

Akiyama *et al.*, (1986) determined that the efficiency of this type of separator was dependent on the annular width of the collection box and the angle and number of vanes used. As the annular gap was increased, collection efficiency was found to be less dependent on the type and number of vanes. A later study by Akiyama and Mauri (1989) of a similar cyclonic separator concluded that the optimum separation distance from the vanes to the collection box was approximately three times the diameter of the vanes.

Larger vanes were shown to swirl the flow more effectively than smaller vanes at a lower pressure drop and angles less than 45 degrees were shown to generate lower centrifugal velocities in the flow.

The first attempt to develop a mathematical model for an inline vortex separator was Ramachandran (1994). Though based on assumptions regarding the flow and multiphase interaction, his model was fairly successful in predicting pressure drops and collection efficiencies. Klujzso *et al.*, (1999) used CFD to further investigate the effects key design parameters of the inline. The variables investigated by Klujzso are the overall diameter, blade geometry, separation distance, collection gap size and airflow velocity. These variables were tested using CFD and verified with physical models. Klujzso concluded that the mechanism for separation of the investigated design offered reasonable efficiency at a lower pressure drop than other available methods of separation. He also concluded that increasing the number of guide vanes increases the pressure drop. He determined that there should be no gaps in projected area of the blades. To prevent detrimental low pressure regions he added front and rear cones on the vane hub. Progressively angled vanes (curved) were shown to offer a lower pressure drop than straight vanes. Klujzso determined that an optimum collection distance and gap distance could be found to maximize efficiency. The physical simulations validated the CFD results.

The lower pressure drop and simplicity of the device proposed by Klujzso make it an attractive choice for a pre-collector in a HMA plant. A similar device could be incorporated into existing ductwork making integration very simple. However, the model tested by Klujzso was quite small (51.8mm diameter) and could only handle very small

airflows (velocities in the range of 4.2 to 6.1 m/s). The nominal airflow for an HMA plant is 67,000 ft³/min. The intent of this study is to adapt this design for the operating conditions and design specifications of an HMA plant using CFD. The following chapters will describe the procedure implemented in this study, results of the CFD analysis, and finally, conclusions drawn from the results.

CHAPTER II

PROCEDURE

The laws which govern the flow of fluid can be mathematically described in a set of equations known as the Navier-Stokes equations. The Navier-Stokes equations are coupled, non-linear, partial differential equations which describe the mass and momentum conservation of fluids. Because of the complexity of these equations, finding an exact solution for them is often impossible unless many simplifying assumptions are made.

Numerical methods offer a means of approximating the solution of the Navier-Stokes equations. However, the large number of calculations required to approximate the solution of more complex problems necessitates the use of computers. The increasing computational speed of modern computers continues to make more and more types of fluid simulations possible.

The segregated solver in Fluent 6.0 solves the equations of continuity, momentum, and energy sequentially. The segregated solver is applicable to incompressible or mildly compressible flow conditions. The control volume method is applied to solve the integral equations for the conservation of mass and momentum. The solution domain is divided into discrete geometric control volumes. Fluent performs the integration of the governing equations on the individual volumes to create a set of algebraic equations for the discrete variables such as velocity and pressure for each control volume. Each of the discrete non-linear governing equations is linearized implicitly with respect to the equation's dependent variable. The result is a linear equation system which is solved iteratively to arrive at the solutions for the discrete

variables at each control volume. A point implicit (Gauss-Seidel) linear equation solver is used in conjunction with an algebraic multigrid (AMG) method to calculate the linear system of equations for each control volume. Values for the variables on the control volumes faces are interpolated.

Each iteration consists of the following steps: first, fluid properties are updated per the current solution. Second, u, v and w components of momentum are solved using the current values of pressure and face fluxes to determine the velocities. Third, a Poisson type of equation is applied to the pressure and velocity to satisfy the continuity equation. Fourth, all other scalar values are calculated. Finally, the solution is checked for convergence, and the steps are repeated until the convergence criteria are met.

The fluid domain was described by constructing a solid model of the geometry in the solid modeling software package SolidWorks. This volume was then meshed with an unstructured tetrahedral scheme using ICMCFD's tetrahedral meshing module and the resulting mesh was imported into Fluent's solver. Boundary conditions were specified, and the solution was run until convergence criteria was met.

As the effects of the geometry are coupled to the performance of the device, it is difficult to isolate a single parameter for investigation. To simplify analysis, first only the vane geometry was investigated by making key construction dimensions parametric. An optimum geometry was selected by the condition of maximum tangential velocity generated at the wall excluding the boundary layer with the minimum pressure drop. Once a particular vane geometry was chosen, other variables were investigated keeping the vane geometry constant.

The variables investigated in this study were vane design (including overall angle, sweep angle, and departure angle), separation distance, annular gap distance, axial gap distance, and vortex tube shape shown in Figure 5. For each geometrical variation the following procedure was completed: (1) the specified geometry was constructed or modified, (2) a new mesh was generated for each variation, (3) a solution was run and allowed to converge, (4) the mesh was then refined by gradients to ensure mesh independence and the solution was iterated until convergence was again met, and finally, (5) the results were recorded and tabulated.

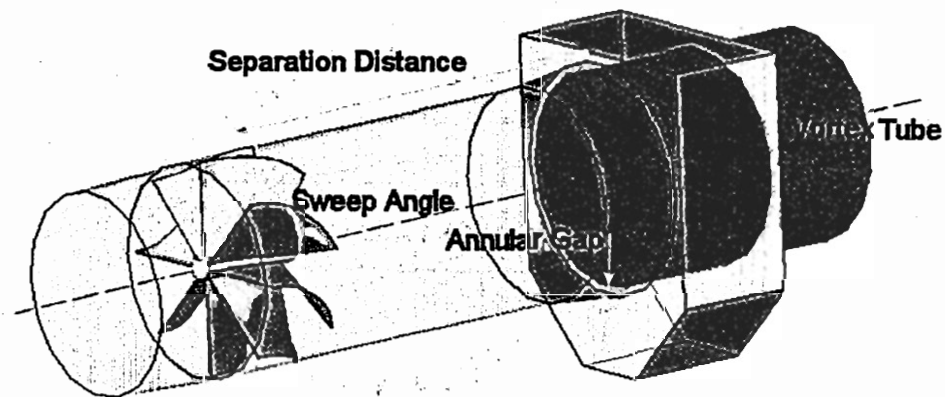


Figure 5. Vortex separator showing key variables and vortex tube (blue)

Turbulence Model

A turbulent flow is characterized by fluctuations in the velocity field. These fluctuations can be very small in scale and potentially high in frequency. To explicitly account for these fluctuations in the Navier-Stokes equations, a method called *direct numerical simulation* (DNS) must be used. The turbulent fluctuations are caused by flow

eddies with a range of length and time scales. The length scale is a physical quantity which relates to the size of the large eddies. For fully developed pipe flow the length scale can be described as $l = 0.07D$, where D is the pipe diameter. The large scales are measured by the characteristic length of the mean flow and the small scales as the dissipation of kinetic energy. The ratio of large to small scales is proportional to $Re_t^{3/4}$. In order to accurately simulate all scales of eddies, the mesh would need to be proportional to $Re_t^{9/4}$. This is computationally beyond reach for the large 3-D geometries of interest in this study.

Because an exact solution is impossible, the instantaneous equations are time averaged to produce a simpler set of equations. This technique is called *Reynolds Average Navier-Stokes* (RANS). RANS decomposes the exact solution of the Navier-Stokes equations into a mean and fluctuating component.

$$u_i = \bar{u}_i + u'_i \quad (1)$$

where \bar{u}_i is the mean velocity component and u'_i is the fluctuating component.

A similar equation can be written for scalar quantities. This averaging process produces the RANS equations.

$$\frac{\partial}{\partial x_i} (\rho u_i) = 0 \quad (2)$$

$$u_j \frac{\partial(\rho u_i)}{\partial x_j} = -\frac{\partial p}{\partial x_i}(\rho u_i) + \frac{\partial \tau_{ij}}{\partial x_j} + \rho g_i + \frac{\partial}{\partial x_j}(-\rho \overline{u'_i u'_j}) \quad (3)$$

$$\tau_{ij} = \left[\mu \left(\frac{\partial u_i}{\partial x_j} + \frac{\partial u_j}{\partial x_i} \right) \right] - \frac{2}{3} \mu \frac{\partial u_i}{\partial x_i} \delta_{ij} \quad (4)$$

where ρ , p , and u are the average density, pressure, and velocity respectively and the subscripts $i, j = 1, 2, 3$ correspond to the Cartesian coordinate components. The body force due to gravity is accounted for in the ρg_i term. The stress tensor term τ_{ij} is further defined in equation (4) where μ is the molecular viscosity and δ_{ij} is the Kronecker delta. The final term in equation (3) is the Reynolds stress term $(-\rho \overline{u'_i u'_j})$. The Reynolds stress term must be modeled to account for the effects of turbulence.

A common method to account for the Reynolds stress term is the Boussinesq hypothesis which relates the Reynolds stress to the mean velocity gradients. The Boussinesq hypothesis is used by the Spalart-Allmaras, k - ϵ and k - ω turbulence models and simplifies the calculation of the turbulent viscosity μ_t by assuming it is an isotropic scalar. The Boussinesq approach adds two additional equations to solve for the turbulent kinetic energy, k , and either the turbulent dissipation rate, ϵ , or the specific dissipation rate, ω . The alternative method is the Reynolds stress model. RSM solves the transport equations for each term in the Reynolds stress tensor. This adds seven additional equations for a 3 dimensional case. Because it has fewer equations to solve, the

Boussinesq approach is a much less computationally costly approach than the RSM. The Boussinesq approach gives the Reynolds stress term to be:

$$-\overline{\rho u'_i u'_j} = \mu_t \left(\frac{\partial u_i}{\partial x_j} + \frac{\partial u_j}{\partial x_i} \right) - \frac{2}{3} \left(\rho k + \mu_t \frac{\partial u_l}{\partial x_l} \right) \delta_{ij} \quad (5)$$

The accuracy of various turbulence models has been investigated for many flow conditions. The models which have been used for cyclone modeling, which involve strong swirling flows, have been the Reynolds stress model (RSM) and the k- ϵ models (Boysan et al., 1982; Griffiths and Boysan, 1996; Ma *et al.*, 2000). While the k- ϵ model is a very robust and widely applicable model, it was shown to be less accurate for swirling flow due to the isotropic turbulent viscosity assumption (Boysan *et al.*, 1982). The RSM model has been shown to be more accurate for swirling flow, but it is considerably more computationally intensive (Ma *et al.*, 2000).

A variation of the k- ϵ model called the Renormalization group method (RNG) was developed to better account for differing flow conditions. The RNG based k- ϵ model provides the accuracy of the RSM model and the simplicity of the standard k- ϵ model. The key difference between the standard k- ϵ and the RNG model is that in the formulation of the RNG model, the calculation of the turbulent viscosity from the solution of an ordinary differential equation takes in to account the effects of rotation and adds an additional term in the dissipation rate transport equation (Griffith and Boysan, 1996).

The turbulent viscosity μ_t for the RNG model is defined as:

$$\mu_t = \rho C_\mu \frac{k^2}{\varepsilon} \quad (6)$$

where $C_\mu = 0.0845$ is a constant defined by RNG theory. The turbulent kinetic energy, k , and the turbulent dissipation rate, ε , are solved from the following transport equations:

$$\rho u_j \frac{\partial \varepsilon}{\partial x_j} = \frac{\partial}{\partial x_i} \left(\alpha_k \mu_{eff} \frac{\partial k}{\partial x_i} \right) + \mu_t S^2 - \rho \varepsilon (1 + 2M_t^2) \quad (7)$$

$$\rho u_j \frac{\partial \varepsilon}{\partial x_j} = \frac{\partial}{\partial x_i} \left(\alpha_\varepsilon \mu_{eff} \frac{\partial \varepsilon}{\partial x_i} \right) + C_{1\varepsilon} \frac{\varepsilon}{k} \mu_t S^2 - C_{2\varepsilon} \rho \frac{\varepsilon^2}{k} - R \quad (8)$$

where

$$\mu_{eff} = \mu + \mu_t \quad (9)$$

$$S \equiv \sqrt{2S_{ij}S_{ij}} \quad (10)$$

$$S_{ij} = \frac{1}{2} \left(\frac{\partial u_i}{\partial x_j} + \frac{\partial u_j}{\partial x_i} \right) \quad (11)$$

$$M_t = \sqrt{k/a^2} \quad (12)$$

$$R = \frac{C_\mu \rho \eta^3 (1 - \eta / \eta_0) \varepsilon^2}{1 + \beta \eta^3} k \quad (13)$$

and constants derived from RNG theory: $\alpha_k=1.393$, $C_{1\varepsilon}=1.42$, $C_{2\varepsilon}=1.68$, $\beta=0.012$, $\eta_0=4.38$, and a is the speed of sound.

Fluent 6 offers a further modification of RNG k- ε model to better account for swirling flow. The equation for the turbulent viscosity is modified to include the effects of swirl.

$$\mu_t = \mu_{t0} f\left(\alpha_s, \Omega, \frac{k}{\varepsilon}\right) \quad (14)$$

where μ_{t0} is the turbulent viscosity calculated without the swirl modification, Ω is a characteristic swirl number determined internally in Fluent, and α_s is a swirl constant which assumes a default value of 0.05 for mildly swirling flow conditions but can be set higher for strongly swirling flow.

Fluent 6 provides the option of using a wall function to simulate the velocity effects in the turbulent boundary layer near wall regions. This eliminates the need for very fine mesh resolution near wall boundaries, greatly reducing computation cost. The wall function satisfies the no slip condition at the wall face and uses the following equations near wall boundaries. The formulation is as follows:

$$U^* = \frac{1}{\kappa} \ln(Ey^*) \quad \text{for } y^* > 11.225 \quad (15)$$

and
$$U^* = y^* \quad \text{for } y^* < 11.225 \quad (16)$$

where

$$U^* \equiv \frac{U_p C_\mu^{0.25} k_p^{0.5}}{\tau_w / \rho} \quad (17)$$

with constants $\kappa = 0.42$ and $E = 9.81$. U_p , y_p , τ_w , and k_p are the mean velocity, distance to the wall, wall shear stress, and turbulent kinetic energy, respectively. The formulation for the production of turbulent kinetic energy and the dissipation rate are also modified in the control volumes near wall boundaries.

Simulation Parameters

The RNG based k- ϵ model was chosen to model turbulence. The vortex separator as illustrated in Figure 4. was considered to be isolated from the total system (Figure 1). Boundary conditions were chosen to best represent standard operating conditions. The energy equation was selected to account for the high temperature, which was set at 270°F to simulate exhaust gases from the drum. The fluid [air] was assigned the ideal gas law to model the change in density due to the temperature. Pressure was assumed to be atmospheric for the inlet. The gravitational force was set to 32.2ft/s² in the negative y direction.

To better simulate operational conditions, a velocity boundary condition was set at the outlet rather than the inlet because the fan is pulling rather than blowing air through the system. The inlet was assigned a pressure inlet boundary condition with a gage pressure of 0 inches of water. Turbulent intensity and hydraulic diameters for the inlet and outlet were calculated for the nominal flowrate, and the temperature was set to be constant. The solution was initialized from the outlet velocity conditions and allowed to converge.

Particle Tracking

Once a converged solution was obtained for the flow field, the collection efficiency of the design was determined by releasing particles and tracking their trajectories. The Discrete Phase Model (DPM) in Fluent can be used to model bubbles, droplets, or inert particles. The fluid and particle phases can be either coupled or decoupled based conditions in the flow field. De-coupling the phases, called *one-way coupling*, assumes that the particle trajectories are determined by the flow field but do not alter the flow as they pass nor do particles interact with each other. These assumptions are desirable because they greatly reduce computation time and are valid if two specific criteria are met.

Lun and Bent (1994) concluded that for particle volume fractions less than 10% the dominant mechanism of momentum transfer is the kinetic mode rather than collision with other particles. Hence, the first criteria to validate one-way coupling is that the particle volume fraction must be less than 10% of the fluid volume. Based on nominal HMA plant operating conditions used in this study a dust volume fraction can be calculated to be less than 0.01%.

The second criteria is that the size of the largest particle diameter must be less than the Kolmogorov length scale (the length scale of the smallest turbulent eddies). Studies such as Goubesbet and Berlemont (1999) suggest that particles with diameters smaller than the Kolmogorov scale have negligible influence on local turbulence. The Kolmogorov length scale is given by equation (18).

$$\eta = \left(\nu^3 / \varepsilon \right)^{1/4} \quad (18)$$

where ν is the kinematic viscosity and ε is the turbulent dissipation rate.

A representative value obtained from the CFD results give a Kolmogorov scale of 6.364×10^{-4} m. The largest particle diameter used in the study was 2.5×10^{-4} m. This is smaller but on the same order of the Kolmogorov scale. While the largest particle diameter is of the same order of magnitude of the Kolmogorov scale, one-way coupling was determined to be a valid assumption given the low volume fraction of particles in the system ($< 0.01\%$).

One-way coupling also assumes that particles have no interaction with other particles. The particles were specified as inert meaning that no chemical reactions or phase change were considered. Fluent predicts particle trajectories by integrating the force balance on the particle in a Lagrangian reference frame.

$$\frac{du_p}{dt} = f_{drag} (u - u_p) + g \frac{(\rho - \rho_p)}{\rho_p} \quad (19)$$

where f_{drag} is the drag force give by

$$f_{drag} = \frac{18\mu C_D Re_p}{\rho_p d_p^2 24} \quad (20)$$

and particle Reynolds number: $Re_p = \frac{\rho d_p |u_p - u|}{\mu} \quad (21)$

and u, ρ , are the fluid velocity (or mean velocity for turbulent flow) and fluid density. Particle properties are shown as u_p, ρ_p, d_p , for particle velocity, density, and diameter, respectively. Fluent allows stochastic particle tracking method called the Discrete Random Walk (DRW) to add in the effect of turbulent fluctuations on particle trajectories.

To speed analysis time, most preliminary dimensional investigations involving particle tracking were performed without the DRW model activated, meaning particle trajectories were computed using the mean component of the velocity only. The DRW model was used with the final design iterations to verify the model and previous results. The addition of the DRW model did not alter collection efficiencies significantly.

The trajectory equations are solved through a stepwise integration by discrete time steps using a trapezoidal integration scheme. Boundary conditions are set to consider the DPM. If a particle encounters a wall it can either be reflected in a collision, or it can be trapped. Reflective boundaries can be assigned a coefficient of restitution (CoR) which determines the nature of the reflection, either perfectly elastic (CoR = 1) or perfectly plastic (CoR = 0) or any where in between. Non-wall boundary conditions such

as inlets and outlets can be assigned as interfaces which allow particles to escape or which trap particles.

In this analysis particles were released from the inlet face. The outlet was set to allow particles to escape while the faces in the collection box were set to trap particles. All other surfaces were set to reflect. In this way, the collection efficiency could be determined by calculating the percentage of particles which were trapped. To investigate the effect of the CoR, values of 1, 0.8, 0.6, and 0.4 were used for the CoR on all reflecting boundaries for the final design iteration.

An investigation of all available methods of non-spherical particle drag calculations was performed for 1900 data points for various shaped particles for a range of particle Reynolds numbers (R. P. Chhabra, *et al.*, 1998). Available methods were compared for error and ranges of applicability. One method investigated was the Haider and Levenspiel model. Haider and Levenspiel is a semi-empirical model which expresses the particle drag as a function of the particle shape factor. The shape factor ϕ , is defined as the ratio of the surface area of a same volume spheres, S_s , to the actual surface area of the particles, s . The results of Chhabra, *et al.* indicate that Haider and Levenspiel satisfactorily predicted drag for particles with values of $\phi > 0.67$. Fluent incorporates the Haider and Levenspiel model as an option in the DPM for modeling non-spherical particles.

$$\phi = \frac{s}{S_s} \quad (22)$$

A sphere has a shape factor of 1. Smaller values of ϕ indicate less sphericity. The Haider and Levenspiel modification is valid for the particle Reynolds number less than

2.6×10^5 . The maximum particle Reynolds number observed from the particle tracking studies was on the order of 500. The drag coefficient C_D from equation (20) is defined according to the Haider and Levenspiel model as the following equations:

$$C_D = \frac{24}{Re_p} \left(1 + b_1 Re_p^{b_2} \right) + \frac{b_3 + Re_p}{b_4 + Re_p} \quad (23)$$

and

$$b_1 = \exp(2.3288 - 6.4581\phi + 2.4486\phi^2)$$

$$b_2 = 0.0964 + 1.5565\phi$$

$$b_3 = \exp(4.905 - 13.8944\phi + 18.4222\phi^2 - 10.2599\phi^3)$$

$$b_4 = \exp(1.4681 + 12.258\phi - 20.7322\phi^2 + 15.8855\phi^3)$$

where ϕ is the shape factor defined in equation (22)

The material of the particles was defined as limestone (density = 135lb/ft³, or 2164.5 kg/m³), a common aggregate used in the production of asphalt. Limestone (calcium carbonate) particles are generally cubic in shape so the shape factor modification for non-spherical particles was set to 0.8. Injections were defined for particle diameters ranging from 250 μm (60 mesh per inch) to 25 μm (500 mesh per inch). Each size was injected separately from the inlet face and the resultant fates were recorded.

Horizontal Cyclone

The analysis of the horizontal cyclone design was performed in much the same way as described for the vortex separator. The geometry was constructed and a mesh

generated. The mesh was imported into Fluent and the nominal flow rate and operating conditions were set as with the vortex separator. The flow field was solved and particle tracking studies were performed. Identical sets of particles were released from the inlet of the horizontal cyclone as were the vortex separator. Particle which passed through the outlet were set to have escaped and particles which impacted the hopper were set to have been trapped. The same settings for non-spherical particles and turbulent fluctuations were used as with the analysis of the vortex separator.

CHAPTER III
RESULTS AND DISCUSSION

A primary diameter was chosen to be 5.167ft to give 3400 fpm (17.45 m/s) for 67,000 ft³/min. Preliminary testing showed that the blade design was the driving factor in changing the flow. It was therefore decided that the blade and hub design be investigated first.

Blade Geometry

The blade geometry was made parametric and solutions were run in order to correlate flow characteristics to the blade geometry. The number of blades was chosen to be eight positioned about a six inch diameter hub. The axial blade length was set at two feet. The geometric variables used were the sweep angle and departure angle shown in Figures 6 and 7. The front and rear cone, as well as the axial blade length, were kept constant.

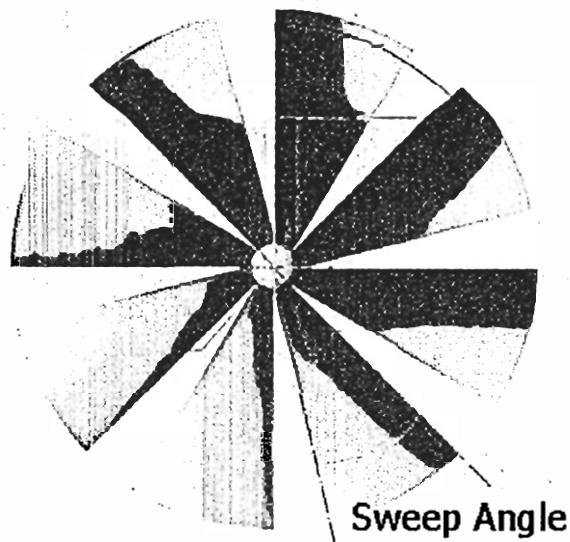


Figure 6. Front elevation of blade and hub geometry showing sweep angle

Departure angles were varied at 45, 50, and 60 degrees. The departure angle correlates to the degree of swirl imparted to the flow by the blades. The sweep angle was varied from 23 to 45 degrees. The physical constraints of the hub and blade geometry limited the sweep angles for the 45 degree departure angle to sweep angles of 23 and 27 degrees. The sweep angle determines to the percentage of the cross sectional area that the blades project onto the flow.

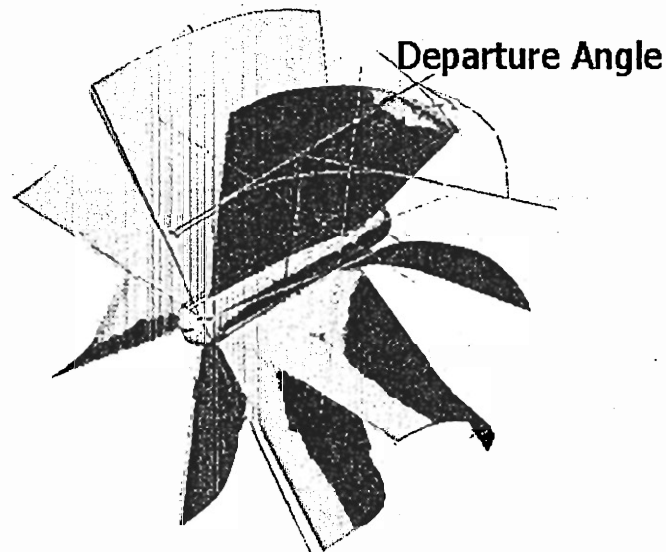


Figure 7. Side elevation of blade and hub geometry showing departure angle.

Only the blades and hub in a shortened section of the duct were considered in this part of the analysis. A constant velocity was set at the inlet and a pressure outlet condition was set on the outlet. The collection box was neglected at this stage of the analysis. Once the solution converged, average surface integrals were taken for pressure on the inlet and outlet to determine the pressure drop across the blades. Average surface integrals were taken for the tangential velocity on the outer wall. The results are shown in Figures 8 and 9.

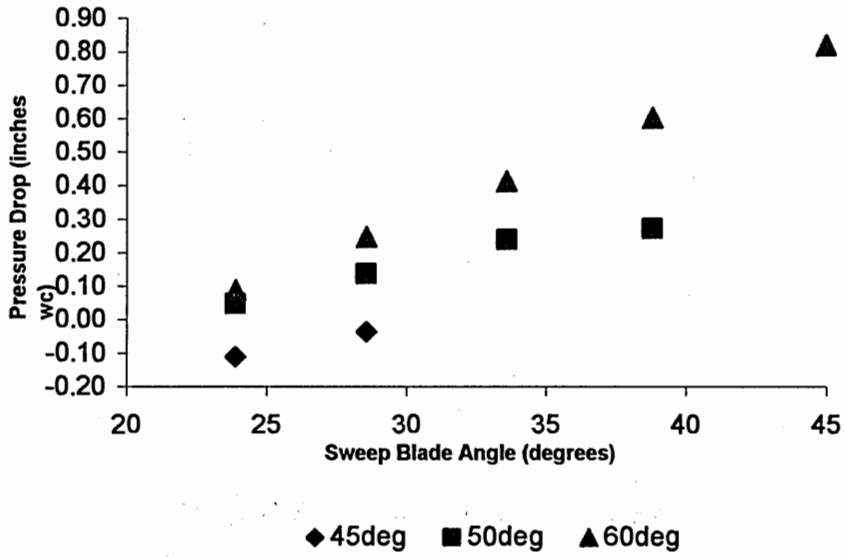


Figure 8. Sweep blade angle versus pressure drop for departure angles 45, 50, and 60°

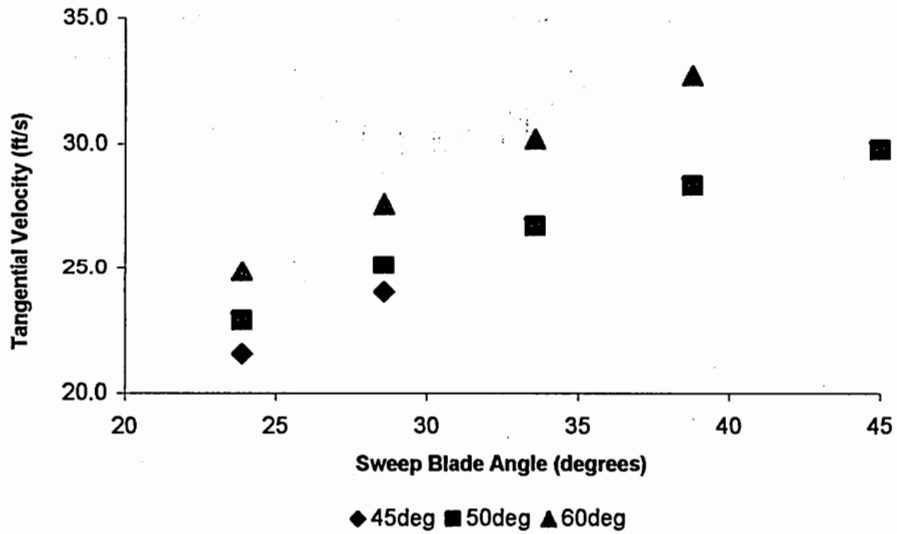


Figure 9. Sweep angle versus tangential velocity for departures angles 45, 50, and 60°

The results in Figure 8 indicate that as the sweep angle increases the pressure drop increases linearly up to a maximum and then levels out. This is consistent with expectation that the pressure drop would increase with increasing sweep angle until the projected area of the vanes completely occludes the flow. Pressure drop also increases with increasing departure angle. The results in Figure 8 look very similar to Figure 9 as the tangential velocity of the flow directly affects the pressure drop. The tangential velocity of the swirling flow will impart a centrifugal force on particles in the flow. Therefore the optimum blade geometry is that which creates the maximum tangential velocity at a pressure drop under the specified limit.

The arbitrarily determined target pressure drop was no more than 1 inch of water (250 Pa) for the entire device. Because the losses associated with the collection box and vortex tube were unknown at this point in the analysis, the blade geometry was chosen to allow for up to 100 Pa of pressure drop to be contributed by the collection box. Thus for no more than $\Delta p = 150$ Pa, the blade geometry with the 60 degree departure angle and the 37 degree sweep angle was chosen. The pressure drop associated with the blades only for this geometry was determined to be 150 Pa.

Flow Results

With a set blade geometry, the full device was modeled to investigate other variables. A general survey of a converged flow field was performed. Figure 10 shows contours of tangential velocity on the midplane. High regions of tangential velocity can be seen immediately downstream of the blades as would be expected. Contours of axial velocity are shown on the midplane in Figure 11. Flow can be seen to accelerate around

the central blade hub. Also it can be seen that there is little to no velocity within the collection box.

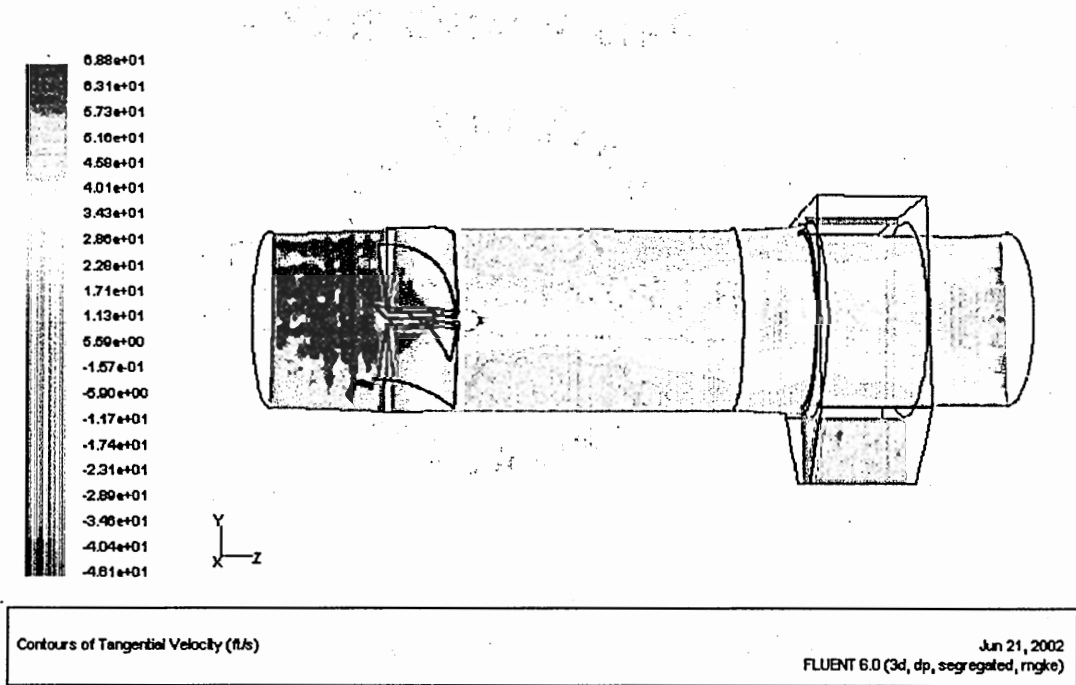


Figure 10. Contours of tangential velocity on midplane

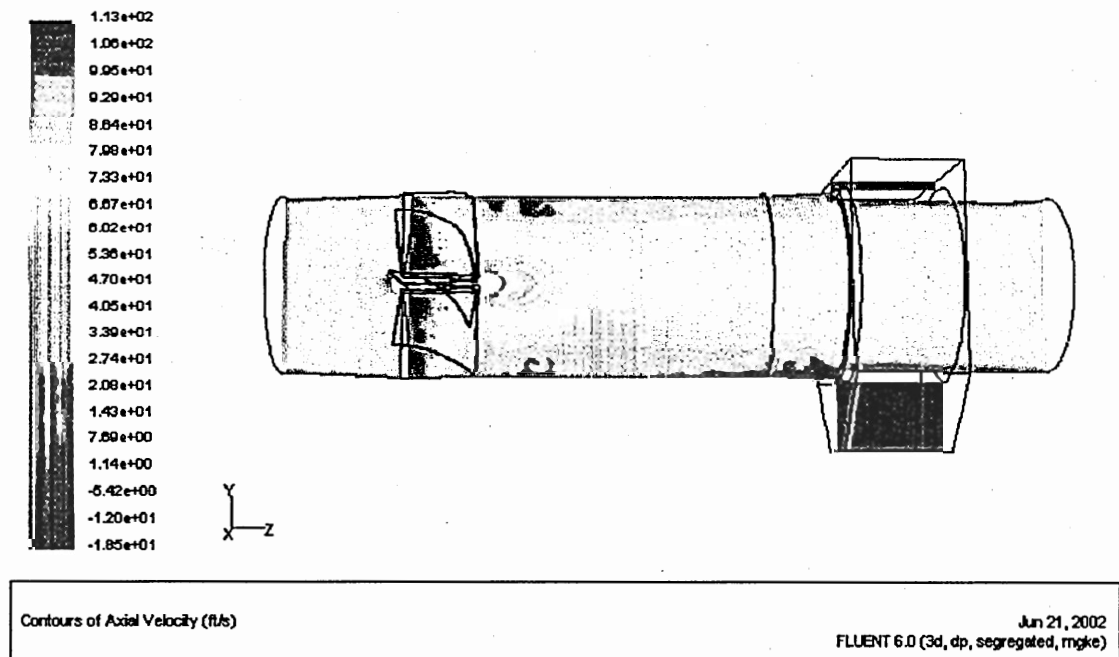


Figure 11. Contours of axial velocity on the midplane

Contours of static pressure in inches of water are shown in Figure 12 on the midplane and the blade and hub surfaces. The low pressure region immediately behind the blade hub can be seen as can a central low pressure region about the axis. Higher pressure regions can be observed on the front of the blades and hub. Figure 13 displays ribbon pathlines released from the inlet. The swirling flow generated by the blades can be easily seen.

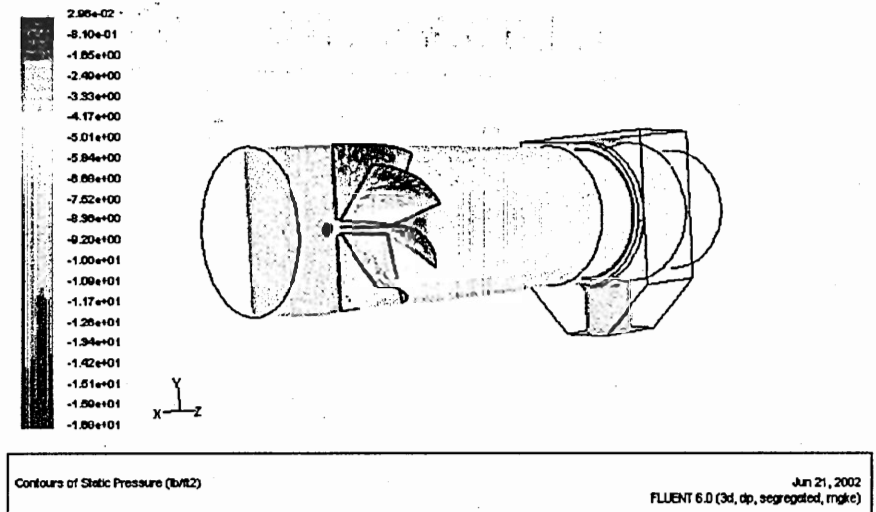


Figure 12. Contours of static pressure in inches of water on the midplane and blades

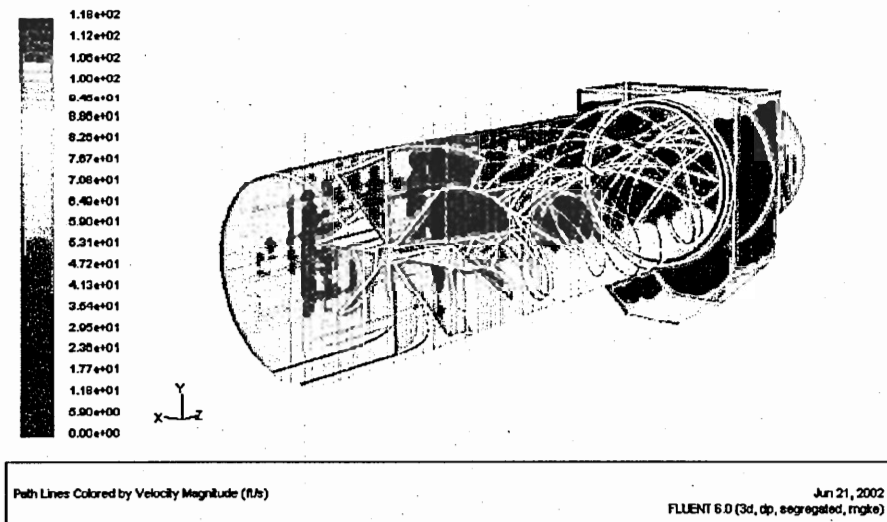


Figure 13. Pathlines release from the inlet colored by velocity magnitude

To gain an understanding of the general behavior of particles in the flow field, single particles were injected into the flow from the inlet. The injection point was varied radially. Two particle sizes were chosen, 150 and 75 μm diameters. The trend shown in Figure 14 indicates that, in general, the larger diameter particles (shown in red) take less distance to move radially out to the wall region than the smaller particles (shown in blue) for the same injection position.

Another observation that can be made is that most particles, except those which enter very close to the center of the inlet, reach the wall in a short distance and proceed to bounce along the wall until they are collected or escape. It also appears that the larger

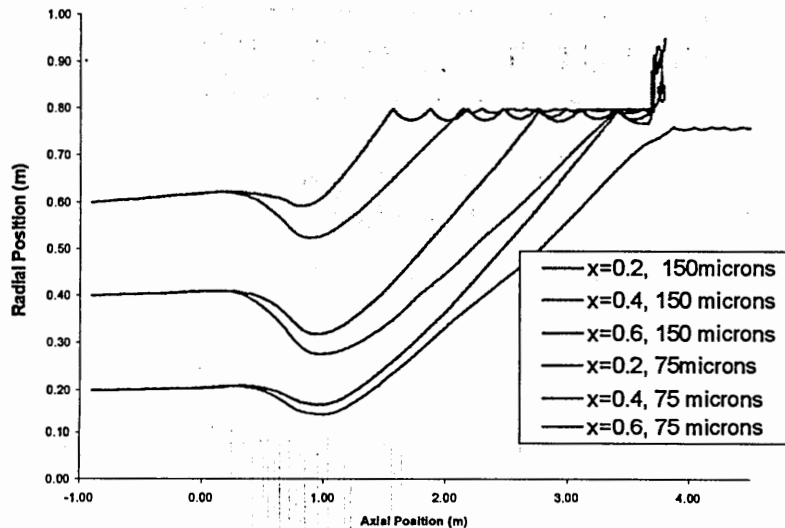


Figure 14. Single injection trajectory tracks for 150 and 75 μm diameter particles

particles with greater mass and momentum rebound farther from their collision with the wall. Accounting for the impact and rebound behavior exhibited by these larger particles is a factor that will be addressed later in this paper.

Grid Study

In any control volume analysis it is critical that the size of the mesh be small enough to resolve the solution accurately. This is particularly important in regions with complex geometry or complex flow characteristics. An infinite number of cells within the fluid domain would ensure the most accurate solution, but this is computationally impossible. Thus, it must be shown that the solution is independent of the mesh resolution. One way this can be done is to monitor scalar results while increasing the mesh resolution. The change of the scalar(s) will decrease as the mesh resolution increases. If the change in the scalar is within a tolerable range, the solution is determined to be independent of the mesh resolution.

For this study, the same methodology was used to generate the tetrahedral mesh for each design iteration. Every effort was made to make each mesh consistent with the others. Local mesh size was specified to enhance resolution in key areas. Areas with enhanced resolution were the blade and hub surfaces and annular gap region.

Because collection efficiency was the key performance indicator, particle tracking was used to determine mesh independence. After convergence, particle tracking studies were performed and the results were recorded. Then the mesh was refined, typically by gradients of velocity to ensure that the resolution in critical regions were adequate. After the mesh was refined it was allowed to converge and more particle tracking studies were performed. If the results of the calculated efficiencies were significantly different further refinements in the mesh were made.

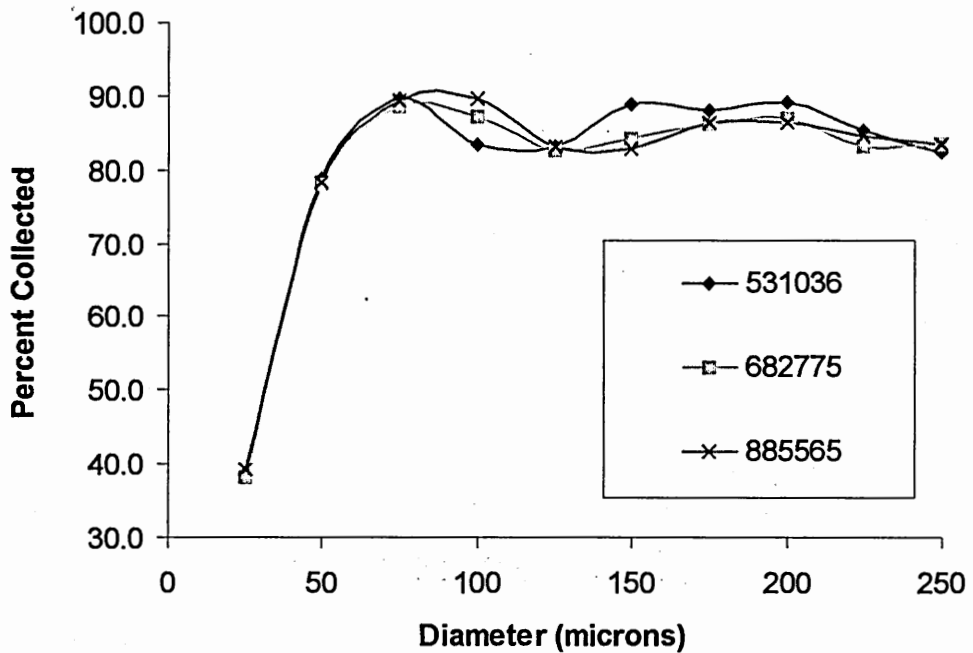


Figure 15. Collection efficiency as a function of cell count

Figure 15 shows a plot of collection efficiency for three levels of refinement with cell counts of 531,036 cells, 682,775 cells, and 885,565 cells. The results show that for the collection efficiency approaches a limit as the cell count increase. Table 1 shows the results of the collection efficiency for each cell count. The difference in collection efficiency as a function of the cell count varies for different diameter particles. The average difference per particle diameter from the first refinement (531,036 cells to 682,775 cells) was 2.44%. The average difference for the second refinement was down to 1.21%. Because the investigation sought to observe general trends in collection efficiency as it related to changes in the geometry, an agreement of less than 5% for each sized particle was determined to be an adequate indication of mesh independence.

Table 1. Results of collection efficiency as a function of cell count

Cell Number (microns)	531036 %trapped	682775 %trapped	difference	885565 %trapped	difference
25	38.7	38.2	1.42	39.2	2.53
50	78.8	78.1	0.55	78.4	0.35
75	89.7	88.5	0.24	89.5	1.13
100	83.5	87.2	6.96	89.8	2.87
125	83.1	82.7	0.11	83.2	0.55
150	89.0	84.4	7.35	82.9	1.77
175	88.2	86.1	2.07	86.4	0.30
200	89.3	86.9	3.45	86.3	0.75
225	85.3	83.3	0.77	84.7	1.63
250	82.3	83.4	1.44	83.5	0.22

Average = 2.44 Average = 1.21

Separation Distance

The separation distance was varied from 4 ft to 9 ft. Particles were injected from the inlet and tracked through the device. Figure 16 shows the relationship between collection efficiency, particle size and separation distance. The data suggests the efficiency increases as the separation distance increases, up to the optimum distance. This optimum distance is determined by the specified particle cut size. Performance requirements stipulate that a minimum percentage of particles smaller than 150 μm be collected. Therefore, 9ft is considered an optimum separation distance to meet the performance requirements. Increasing the separation distance further would only increase the percentage of particles smaller than 150 μm collected.

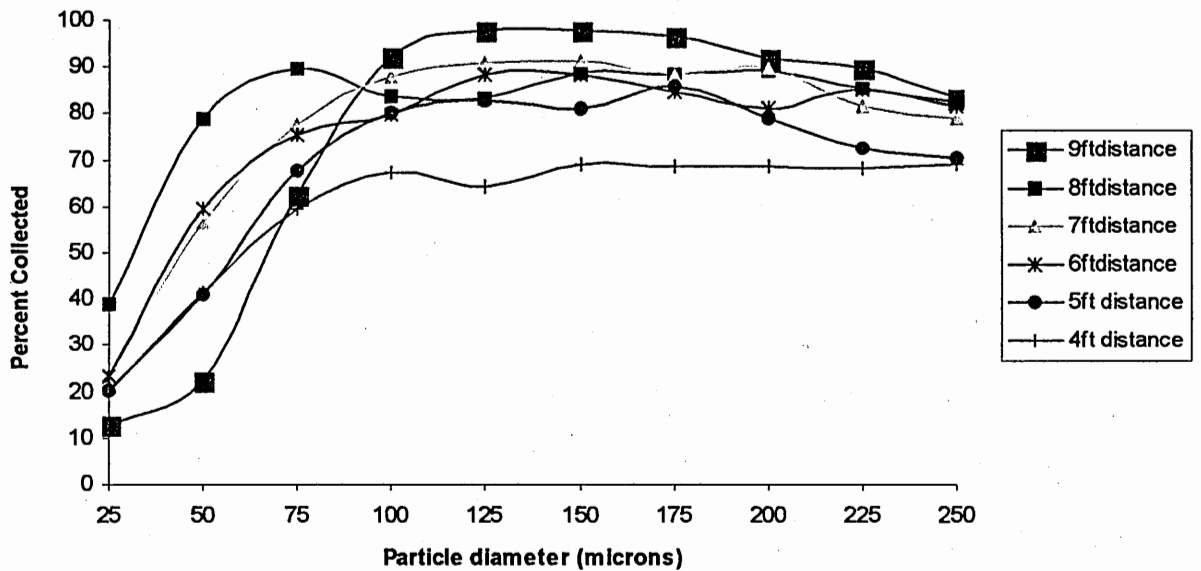


Figure 16. Collection efficiency as a function of separation distance

Annular Gap Distance

The annular gap distance (illustrated in Figure 5) was varied from 1.5 inches (38.1mm) to 3 inches (76.2mm) holding the diameter of the main duct constant. A similar analysis was performed as with the separation distance. Particles were injected from the inlet, and their fates were tracked and recorded. The results are shown in Figure 17. The results show that, in general, as the collection gap increased, efficiency also increased. This is reasonable as the projected escape area increases with the growing gap. However because the main duct diameter was held constant, change of the annular gap required the diameter of the vortex tube to decrease. This reduced the projected outlet area which caused the pressure drop to increase.

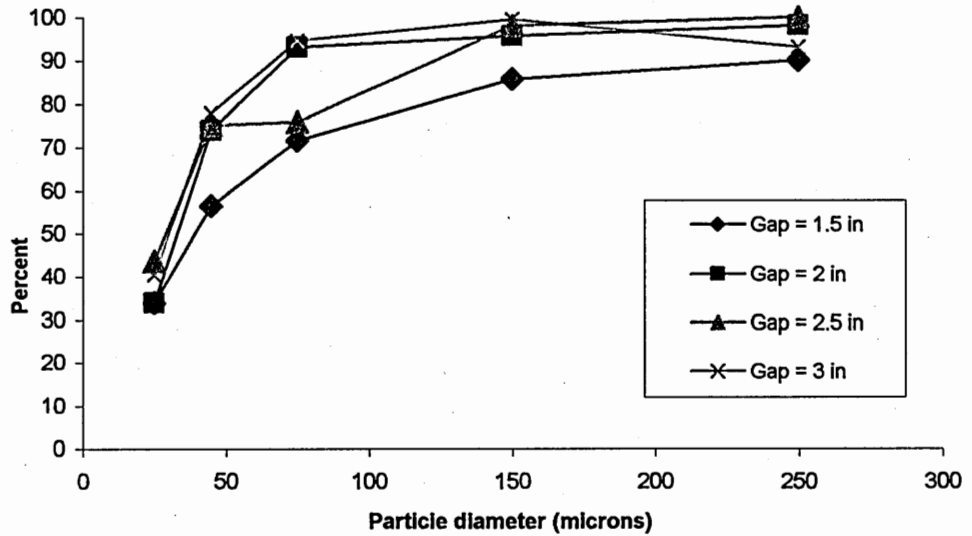


Figure 17. Particle efficiency as a function of annular gap distance

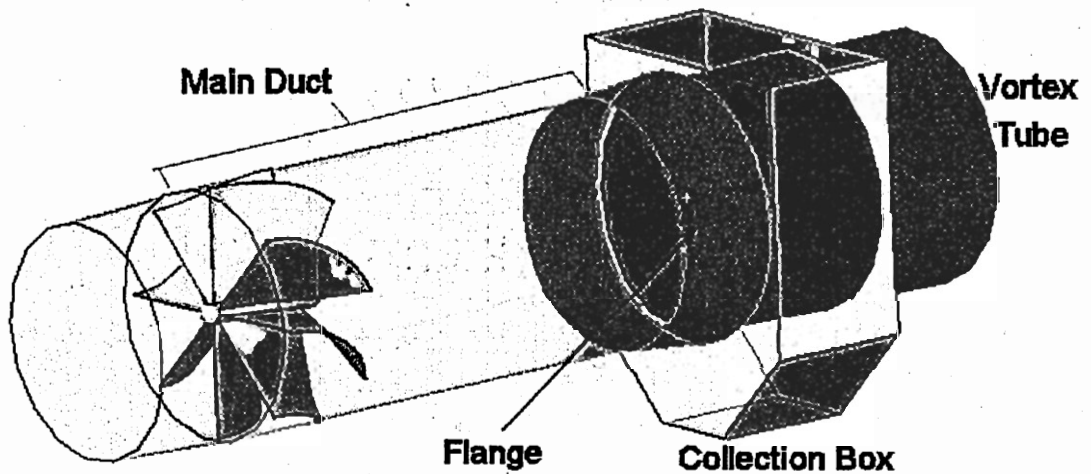


Figure 18. Device showing flange section (in green) next to collection box

An alternative method of increasing the annular gap without affecting the outlet area is to flange the main duct diameter near the inlet to the collection box. This flange

is a conic section attached to the collection box is shown in green in Figure 18. A side elevation detail showing the annular gap is illustrated in Figure 19.

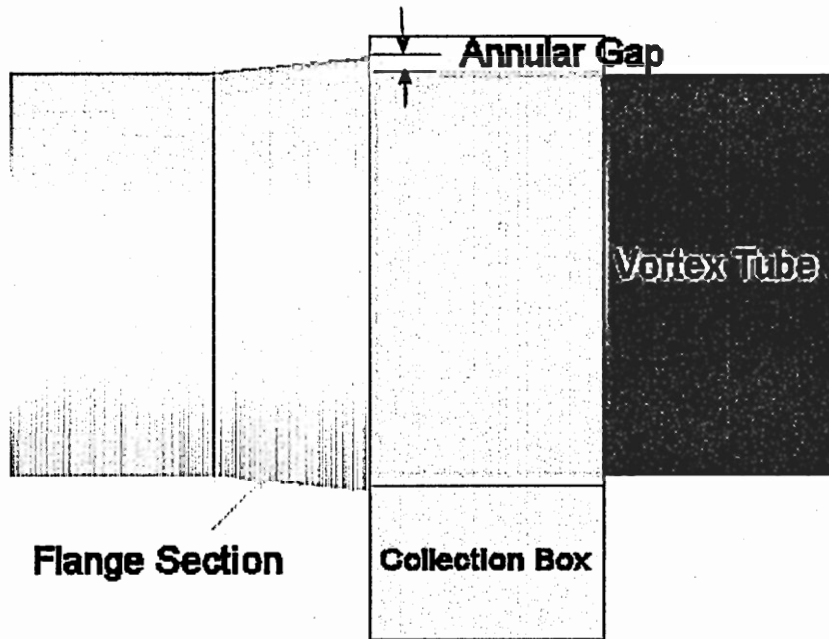


Figure 19. Side elevation detail of flange section showing annular gap

The axial length of the flange section is 2 ft with a radial increase of 2 inches over the main duct diameter of 5ft 2 inches. This provides an effective annular gap of 4 inches while maintaining the outlet diameter of 5ft. The effects of the flange section on collection efficiency can be seen in Figure 20.

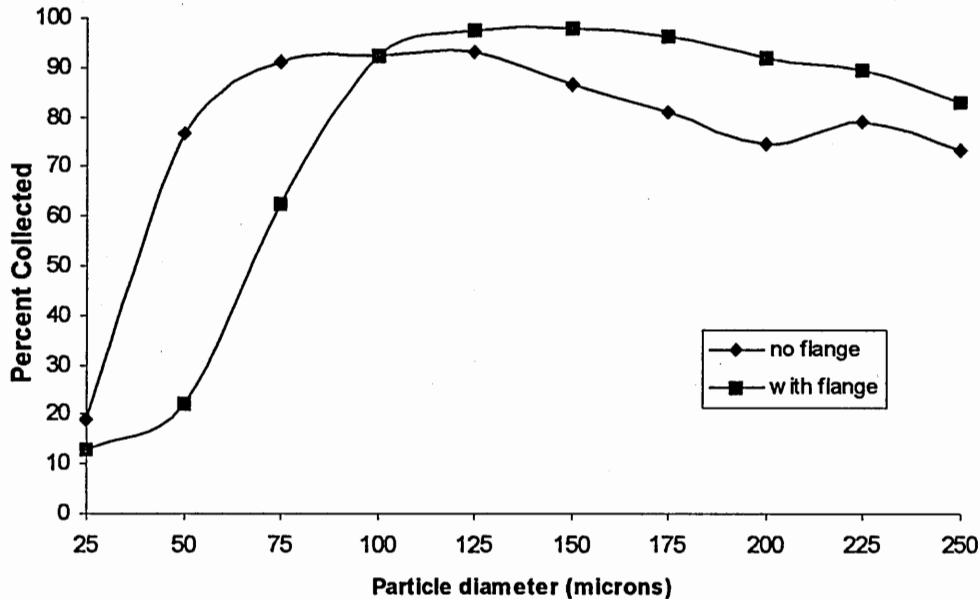


Figure 20. Effect of flange section on collection efficiency

The results show that the flange section provides higher collection efficiencies for particles larger than 100 μm in diameter and poorer efficiency for particles smaller than 100 μm in diameter than the non-flanged geometry. This difference in the collection of larger particles can be attributed to the larger annular gap afforded by the flange which allows more particles to be separated and the increase in radial distance which encourage larger particles which are rebounding from the wall to be collected. The decrease in the collection efficiency of smaller particles observed in the flanged geometry can be attributed to the subtle change in pressure and velocity fields in the region of the annular gap. Figures 21 and 22 display contours of axial velocity on the midplane in the annular gap region for the non-flanged and flanged geometry, respectively. Similarly, contours of static pressure for the non-flanged and flanged geometry are displayed in Figures 23 and 24.

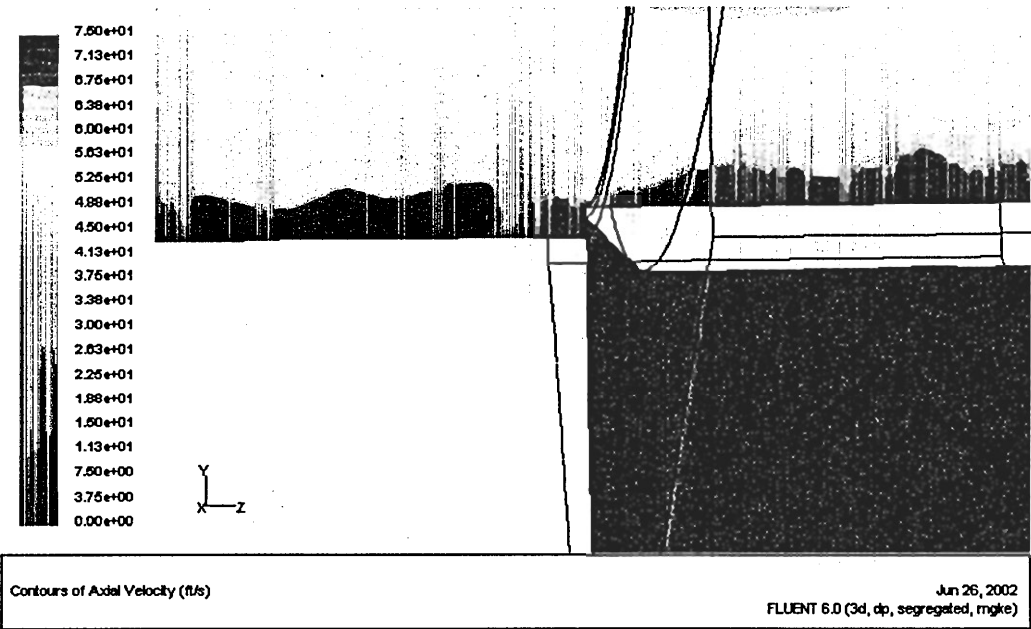


Figure 21. Contours of axial velocity on midplane for non-flanged geometry.

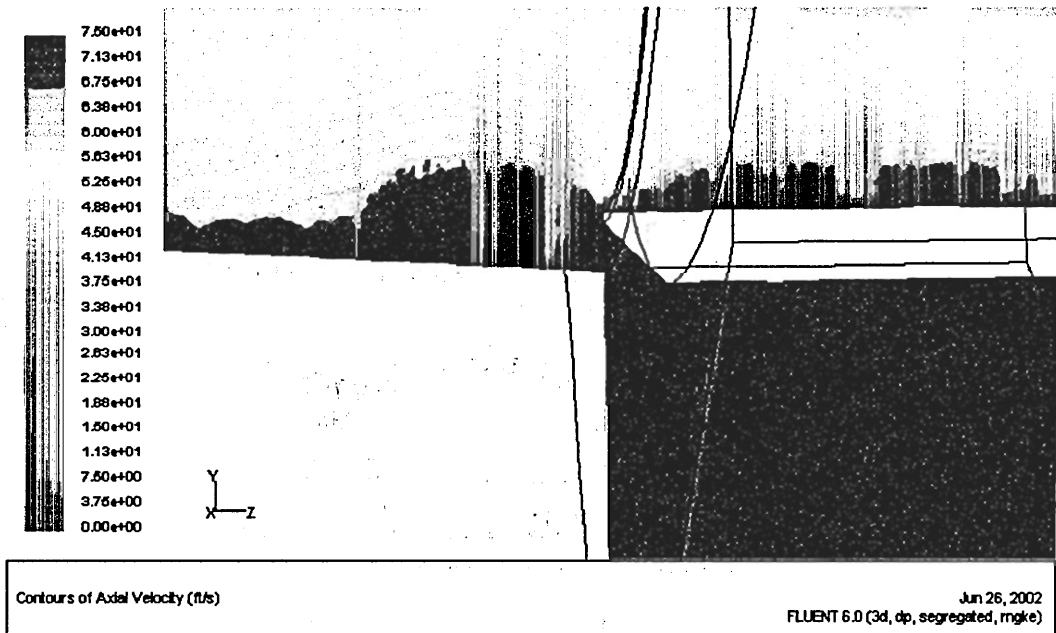


Figure 22. Contours of axial velocity on midplane for flanged geometry.

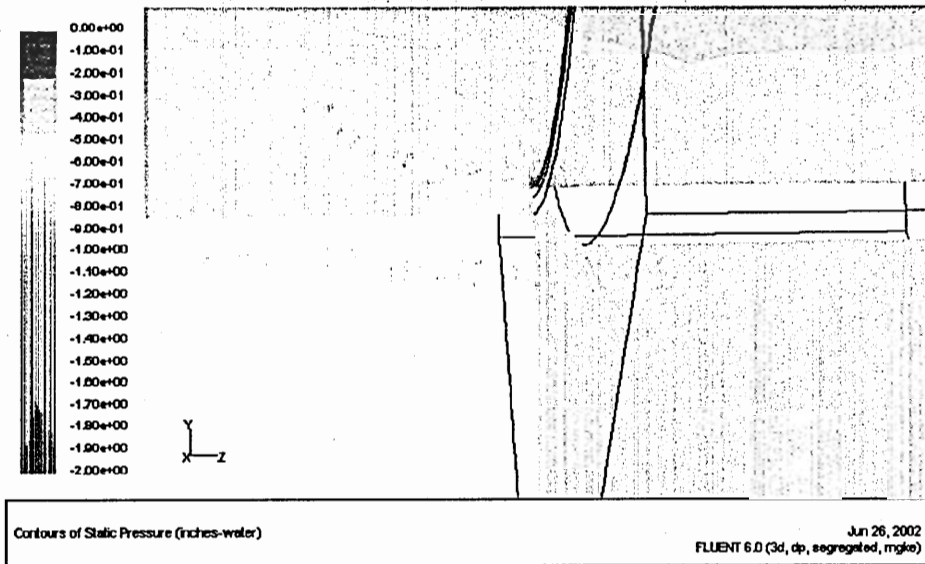


Figure 23. Contours of static pressure on the midplane for non-flanged geometry

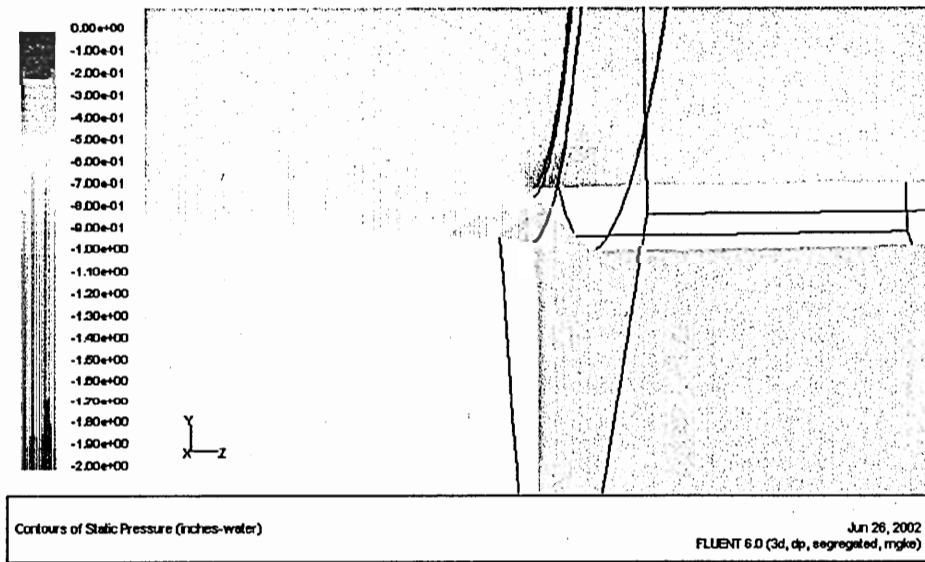


Figure 24. Contours of static pressure on the midplane for the flanged geometry.

Comparison of the pressure and velocity contours show that the flanged geometry provides a slightly higher pressure and lower axial velocity in the region of the annular gap than the non-flanged geometry. This Bernoulli effect causes smaller particles with

less momentum to avoid this higher pressure and lower axial velocity region in the flanged geometry and are consequently not collected. Larger particles with greater momentum are less affected.

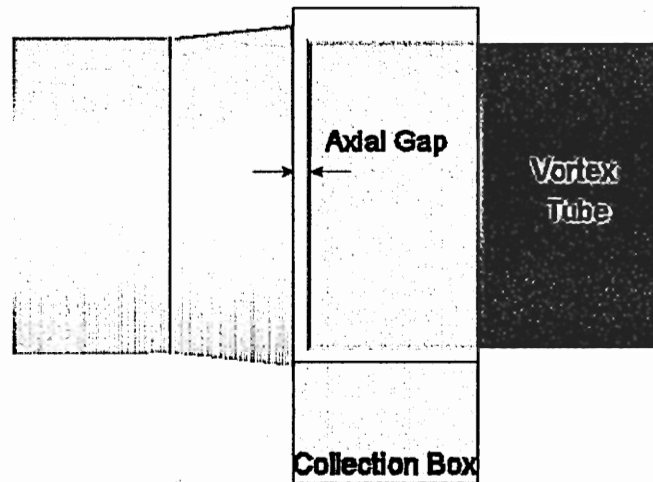


Figure 25. Side elevation showing axial gap detail

Axial Gap Distance

A variable which was not investigated by Klujzso (1999) was the distance from the vortex tube to the front of the collection box as illustrated in Figure 25. This distance is perpendicular to the collection gap. The distance of this axial gap was varied to investigate the effect on collection efficiency. The dimensions assigned to this variable were as follows: 0 axial gap indicates that the vortex tube was even with the collection box, 1 to 3 inches axial gaps were varying degrees of distance that the vortex tube was backed away from the front face of the collection box leaving the gap, and -0.5 inch axial gap refers to the vortex tube moving the opposite direction toward the blades. The results for the collection efficiency are shown in Figure 26. In general, for smaller particles

sizes, collection efficiency was shown to improve with increasing axial gap with the exception of the 1 in axial gap, but no clear trend can be observed for particles larger than 100 μm in diameter.

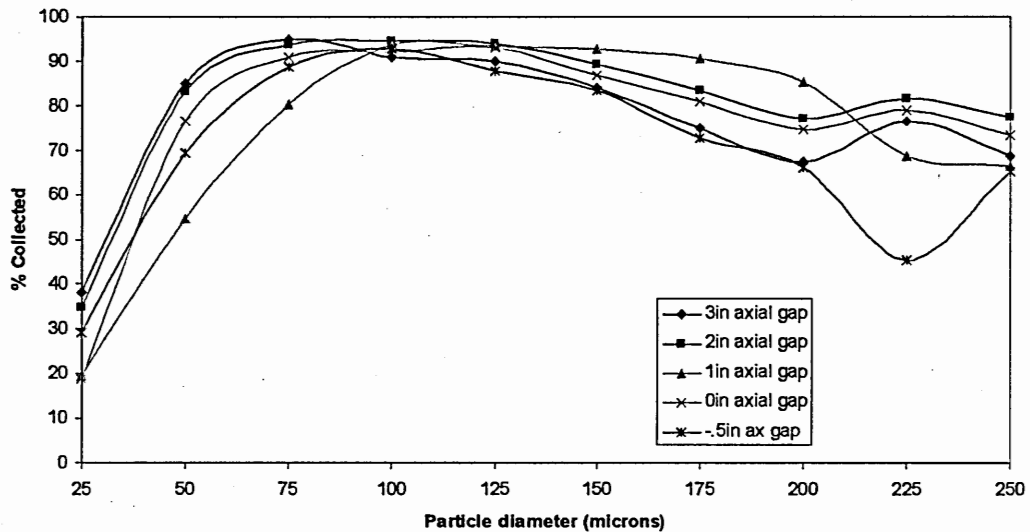


Figure 26. Collection efficiency as a function of axial gap distance.

Because the axial gap variance showed no clear increase in efficiency for larger particles, the geometry was set with no axial gap. Figure 27 shows the efficiency curve for the final design iteration. It shows high efficiencies for particles greater than 100 μm in diameter and decreasing efficiencies for particles smaller than 100 μm in diameter.

Discrete Phase Modifications

With the geometric dimension established, the effects of turbulence were included into the particle tracking. The DRW model was activated to include the turbulent fluctuations in the particle trajectory calculations. Figure 27 shows the collection efficiency of the device for particle trajectories calculated with and without the DRW

model. The turbulent fluctuations seem to have little to no effect on particles larger than 150 μm in diameter. The effect on particles smaller than 150 μm in diameter is an average of 25.3% increased collection efficiency for the DRW model. The results can be seen in Table 2.

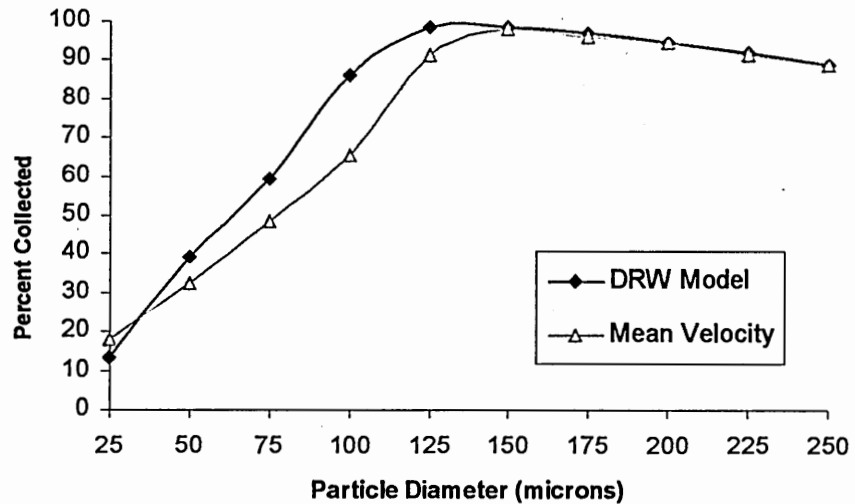


Figure 27. Final design collection efficiency showing DRW model and mean velocity

Table 2. Results of DRW and mean velocity particle tracking

Particle Diameter (μm)	Collection Efficiency		Difference (%)
	Mean	DRW	
25	18.30	13.65	25.38
50	32.25	39.30	21.87
75	48.46	59.11	21.98
100	65.40	86.31	31.98
125	91.12	98.21	7.78
150	97.83	98.23	0.42
175	95.83	96.70	0.90
200	94.29	94.47	0.18
225	91.12	91.57	0.49
250	88.59	88.84	0.29

The final variable investigated was the coefficient of restitution. All particle trajectories calculated up to this point had assumed a perfectly elastic collision ($\text{CoR} = 1$)

with wall boundaries. Because many particles appear to reach the tube wall before the collection box, the nature of the collision(s) with the tube wall affects the particle trajectories and also the resulting collection efficiency of the device.

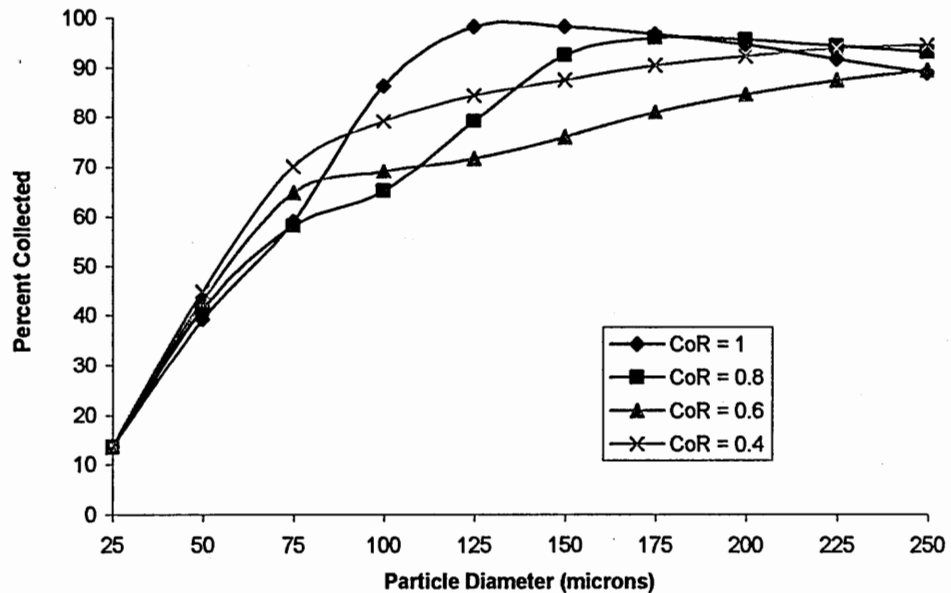


Figure 28. Collection efficiency for varied coefficient of restitution

To determine the effect of the particle-wall collisions, the CoR was varied from 0.4 to 1. The results shown in Figure 28 indicate three distinct characteristic regions which depend on particle diameter. The first characteristic behavior is exhibited by particles smaller than 75 μm . These particles are little affected by changes in the value of the CoR. This is largely due to the fact that most of these particles do not interact with the wall.

The second characteristic behavior is seen in particles in the range of 100-175 μm . High values of the CoR increase collection efficiency. As the CoR decreases, collection efficiency also decreases until the lowest value of CoR (0.4) which in contrast increases the efficiency. For this range of particle diameters, maximum efficiencies occur at the extreme values of CoR. Particles which impact the wall and remain close to the wall are likely to be collected, but particles which collide elastically are also likely to be collected for this range of sizes.

The third characteristic behavior is exhibited by particles larger than 200 μm . In this range of particles, decreasing the CoR increased the collection efficiency. This is because the larger particles tend to reach the wall region and bounce along the surface. Elastic collisions allow the particles to bounce higher and therefore they have a tendency to escape collection. More plastic collisions keep the bouncing particles closer to wall where they are more likely to be collected.

Horizontal Cyclone Results

As suspected, the flow field inside the horizontal cyclone differs from a reverse flow cyclone. Flow enters the inlet circling the vortex tube but is forced away from the vortex tube by the blocking plate. Instead of a strict swirl about the axis, the flow follows a more cork-screw like path. Figure 29 shows pathlines from the inlet. Tangential velocity peaks as flow passes under the vortex tube as shown in Figure 30.

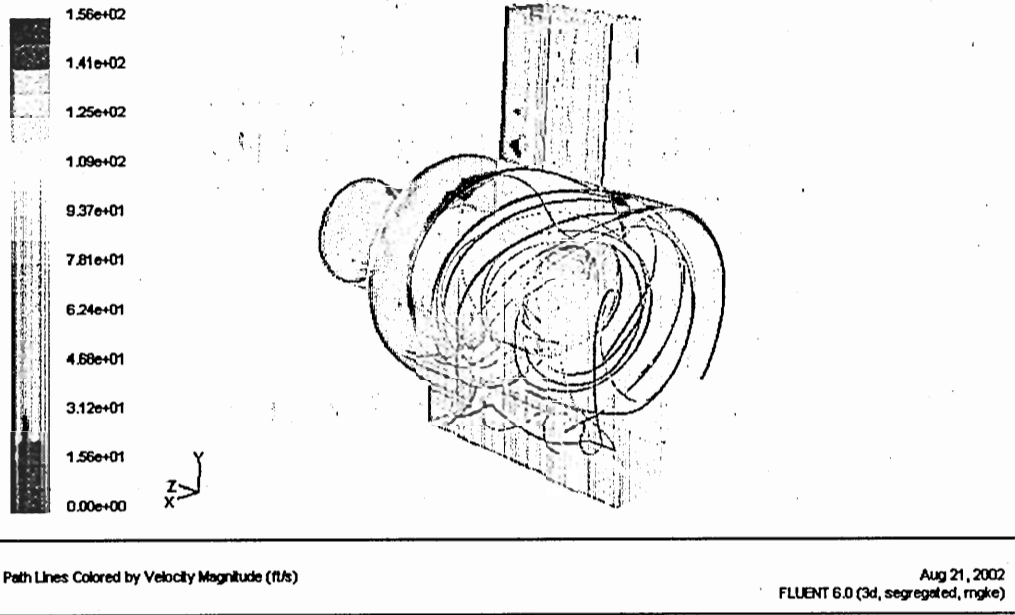


Figure 29. Horizontal cyclone showing pathlines released from the inlet.

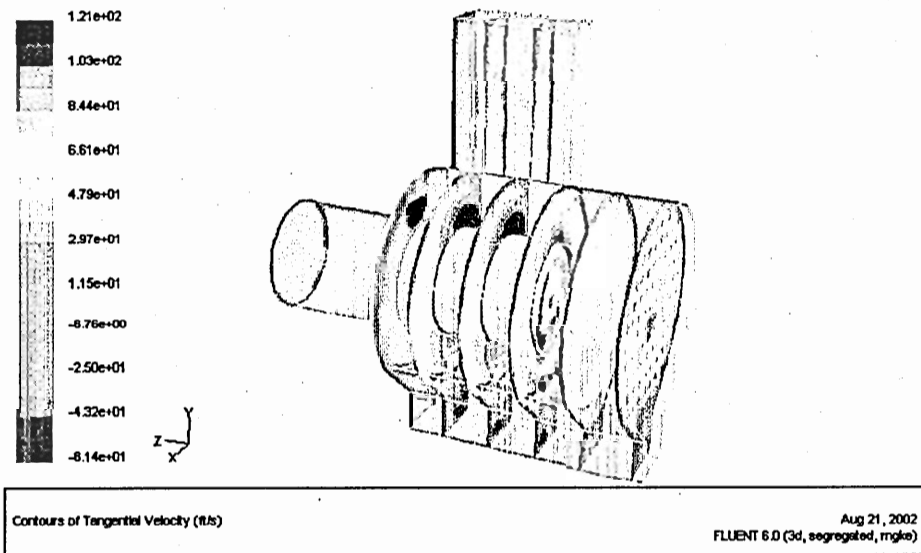


Figure 30. Horizontal cyclone showing contours for tangential velocity

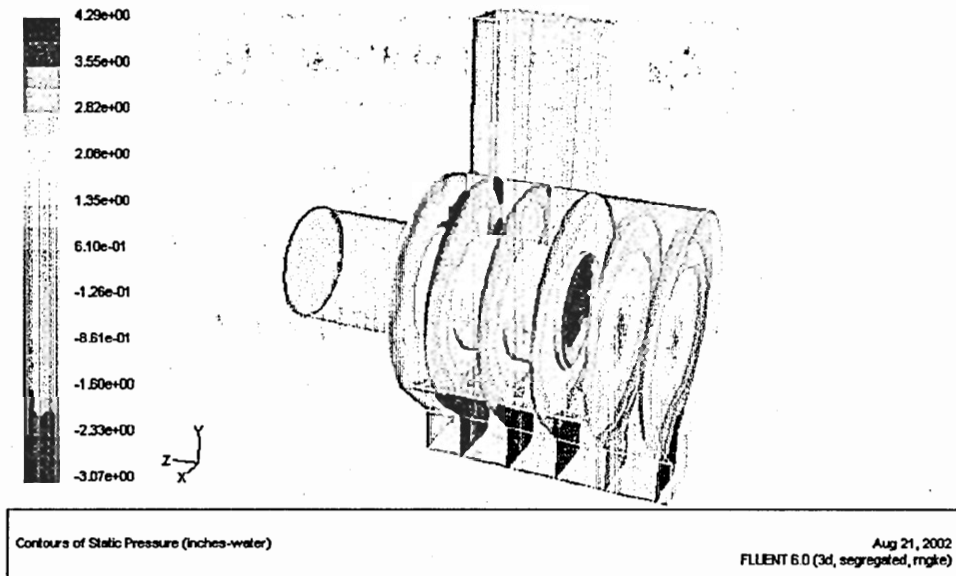


Figure 31. Horizontal Cyclone showing contours of static pressure

The central low pressure region about the axis of rotation can be seen in Figure 31. The predicted pressure drop across the device for the nominal flow rate of 67,000 ft³/min was calculated to be 2.67 inches of water column which compares well to the experimentally measured pressure drop of 3 inches of water.

The results of the particle tracking studies are slightly more difficult to interpret than the vortex separator. It appears that a certain quantity of particles remains entrained in the flow after even after the majority of particles have escaped or been collected. The variables given to Fluent for particle tracking include the step size for each particle trajectory calculation and the total number of steps. The physical interpretation of increasing the number of steps is to track the particle for a longer period of time. Table 3. shows that even doubling the number of steps, no significant change was made to the number of incomplete particles.

Table 3. Results of incomplete particles for 10,000 and 20,000 steps for 125 μm particle

Step Size (ft)	Step Number	Diameter (microns)	Escaped	Trapped	% Collected w/o incomplete	Incomplete	% Collected w/ incomplete
0.0328	10000	125	12	35815	99.967	14293	71.46
0.0238	20000	125	5	35777	99.986	14338	71.38

Because these resident particles are neither trapped nor escaped, a different means must be devised to account for them in the calculation of the collection efficiency of the device. One possible method is to neglect them entirely. Table 4 is the results of all particle diameters for 10,000 steps. The sixth column is the calculated efficiency neglecting the incomplete particles. An alternate method to account for the incomplete particles is to consider them to have escaped. While this is strictly not true it does provide the most conservative estimate of collection efficiency. This calculated efficiency is found in the last column of Table 4.

Table 4. Particle tracking data for 10,000 steps

Step Size (ft)	Step Number	Diameter (microns)	Escaped	Trapped	% Collected	Incomplete	% Collected of Total
0.0328	10000	25	45658	4448	8.88	14	8.87
0.0328	10000	50	15528	18143	53.88	16449	36.20
0.0328	10000	75	1101	37358	97.14	11661	74.54
0.0328	10000	100	31	46037	99.93	4052	91.85
0.0328	10000	125	12	35815	99.97	14293	71.46
0.0328	10000	150	0	38630	100.00	11490	77.08
0.0328	10000	175	0	44419	100.00	5701	88.63
0.0328	10000	200	0	44236	100.00	5882	88.26
0.0328	10000	225	6	44066	99.99	6048	87.92
0.0328	10000	250	40	44541	99.91	5539	88.87

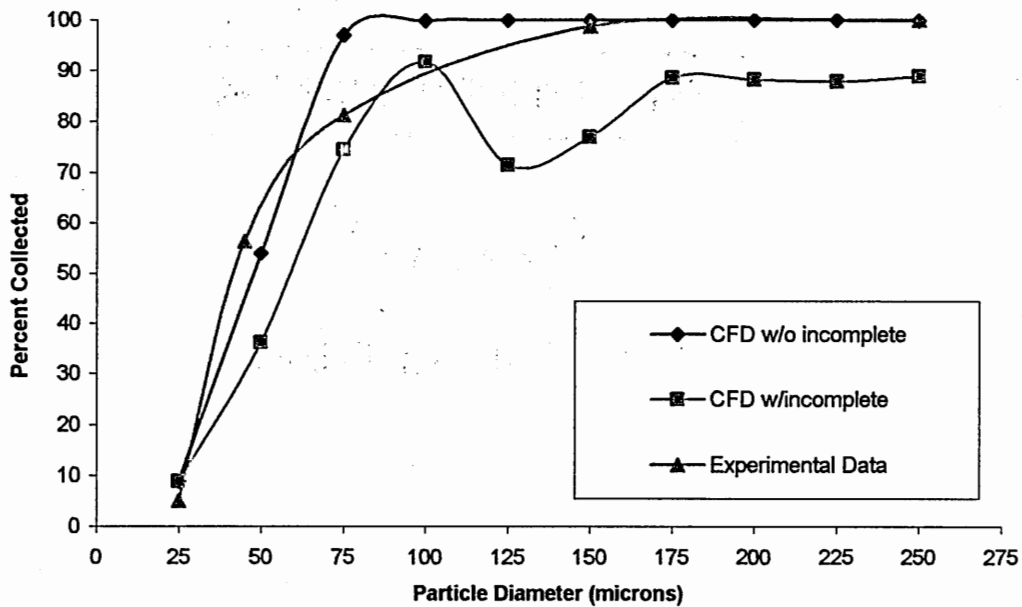


Figure 32. Predicted collection efficiency and experimental data for horizontal cyclone

Both methods are plotted in Figure 32 along with experimental data taken from dust samples removed from an operational horizontal cyclone. The experimental data falls between the two methods for smaller particles but closely matches the predicted results of the first method for larger particles. The experimental data suggests that many of the particles which are considered incomplete by the particle tracking algorithm may eventually be collected. In turn, some of the incomplete particles may escape over time. It is possible that during normal operation a certain quantity of dust is constantly entrained in the flow within the horizontal cyclone.

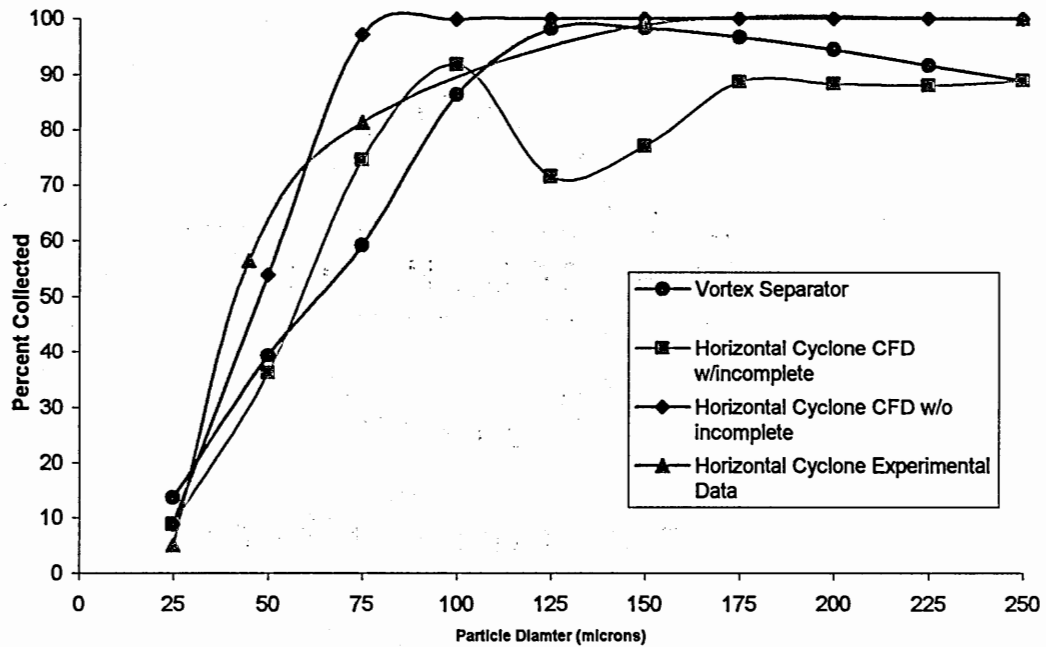


Figure 33. Predicted efficiencies for vortex separator and horizontal cyclone

In Figure 33 the collection efficiency curve of the final design iteration of the vortex separator is added to the previous plot (Figure 32). It can be seen in that the vortex separator falls within the bounds of the two methods of determining efficiency of the horizontal cyclone. The efficiency for the vortex separator drops off sharply at particles smaller than 125 μm in diameter. A similar drop can be seen in the horizontal cyclone at 75 μm . Minimal collection of particles smaller than 150 μm is desirable, therefore the vortex separator can be judged to provide more focused separation for smaller particles than the horizontal cyclone. The vortex separator design shows poorer collection efficiency for larger of particles; however, the collection efficiency is within the bounds set by the two methods of determining the efficiency from the CFD prediction of the horizontal cyclone.

CHAPTER IV

CONCLUSION

The inline cyclonic separator was optimized for the specific design requirements unique to operation as a pre-collector in a HMA plant using CFD. A diameter of 5.167ft was chosen to provide a nominal flowrate. An optimum blade geometry was chosen to generate the maximum tangential velocity at the minimum pressure drop. With this particular blade geometry, the effects of key geometric parameters on collection efficiency were investigated. These parameters were the separation distance, annular gap, axial gap, and the effects of a flanged duct.

Optimum dimensions were determined for each of these parameters to meet the original design specifications: maximum efficiency for particles greater than 150 μm in diameter and minimum efficiency for particles smaller than 150 μm in diameter. The optimum separation distance was determined to be 9 ft. A flanged transition into the collection box was shown to improve collection efficiency by increasing the annular gap to 4 inches without restricting the projected area of the outlet. This flanged section was shown to increase the efficiency of particles larger than 100 μm in diameter. No discernable trend was observed for variance of the axial gap, and therefore it was not included in the final design iteration.

Particle trajectory tracking was performed for a range of sizes of limestone particles for each design iteration using the Haider and Levenspiel model for non-spherical particles. The collection efficiency was determined by the percentage of particles that were trapped in the collection box. The system pressure drop was found to

be 0.52 inches of water (130 Pa), well below the original design specification of 1 inch of water.

The effects of particle-wall impacts were investigated by varying the coefficient of restitution (CoR). Low values of CoR indicating more plastic collisions were shown to increase the collection efficiency for larger particles. Higher values of the CoR indicating more elastic collisions were shown to increase collection efficiency for particles in the 100-150 μm diameter range while decreasing efficiency for the largest of particle sizes.

Because the Haider and Levenspeil model does not consider particle orientation and the orientation of a non-spherical particle would certainly affect particle-wall collisions, the varied collection efficiencies for different values of CoR provide a range of possible particle-wall interactions and the resulting collection efficiencies. Given the limitations of the model, the effects of these varied particle-wall interactions may be the best possible way to predict the effects of irregular shaped particle-wall collisions. It is probable that experimentally obtained collection efficiencies for irregular shaped dust particles may be represented by an average of the collection efficiency curves representing different values of the CoR.

The existing horizontal cyclone currently used in typical HMA plants was modeled and the flow field was calculated. Particle tracking studies were performed using the same criteria established for vortex separator. Predicted collection efficiencies were shown to resemble experimental data taken from collected dust samples. The predicted pressure drop across the device was approximately 10% lower than the experimentally measured value.

In conclusion, the predicted performance of the final design iteration meets the operational requirements of a HMA plant primary collector. Collection efficiencies were shown to be comparable to that of the existing horizontal cyclone design. The pressure drop across the device was shown to be approximately 1/6 that of the horizontal cyclone design currently in use. The predicted collection efficiency provides satisfactory performance over a range of values for variables including the shape factor and the CoR. The use of these two variables make the particle trajectory calculations more representative of real world operating conditions.

APPENDIX A

Blade Geometry Data

Configuration	Departure <	Radial Length	Axial Angle	Inlet P	Outlet P	Delta P	Tang V	Rad V	Axial V
	(degrees)	(inches)	(degrees)	(pascals)	(pascals)	(pascals)	(m/s)	(m/s)	(m/s)
45deg11in	45	11	23.9	-25.970	0.815	-26.786	6.571	0.577	17.762
45deg13in	45	13	28.6	-8.581	0.861	-9.442	7.320	0.589	17.581
45deg15in	45	15	33.6	-9.584	0.861	-10.445	6.975	0.582	17.589
50deg11in	50	11	23.9	-10.006	0.862	-10.868	6.975	0.585	17.593
50deg13in	50	13	28.6	11.910	1.301	10.609	7.659	0.638	17.582
50deg15in	50	15	33.6	36.361	1.133	35.228	8.160	0.604	17.449
50deg17in	50	17	38.8	61.059	1.154	59.905	8.646	0.613	16.864
50deg19in	50	19	45	69.205	1.189	68.016	9.077	0.620	16.514
60deg11in	60	11	23.9	21.614	1.043	20.571	7.577	0.676	16.840
60deg13in	60	13	28.6	64.178	1.175	63.003	8.421	0.602	16.971
60deg15in	60	15	33.6	105.790	1.286	104.504	9.213	0.632	16.436
60deg17in	60	17	38.8	153.441	1.596	151.845	9.986	0.642	16.049
60deg19in	60	19	45	207.302	3.482	203.820	10.842	0.767	15.765

APPENDIX B

Collection Efficiency for Varied Annular Gap

60deg17inA9ft15gap

Shape Factor		1	0.8	0.6
Mesh Size	Diameter			
60	250	65	90	68
100	150	90.4	85.7	64.6
200	75	81.7	71.7	58.9
325	45	61.7	56.5	50.1
500	25	37.7	34	26.4

60deg17inA9ft2gap

Shape Factor		1	0.8	0.6
Mesh Size	Diameter			
60	250	78	98	85.2
100	150	96.6	95.7	84
200	75	95.7	93.2	75.3
325	45	80.3	74.1	59.2
500	25	38.2	34	28.4

60deg17inA9ft25gap

Shape Factor		1	0.8	0.6
Mesh Size	Diameter			
60	250	98.2	100	85.8
100	150	100	98.1	76.3
200	75	79	76	72.8
325	45	70.1	75.2	67.5
500	25	51.7	43.8	38.9

60deg17inA9ft3gap

Shape Factor		1	0.8	0.6
Mesh Size	Diameter			
60	250	89	93	98
100	150	98.4	99.5	98.13
200	75	94.9	94.6	91.7
325	45	81.5	78.1	70.1
500	25	44.5	40.5	33.7

APPENDIX C

Collection Efficiency for Varied Separation Distance

Separation Distance	6ft			7ft		
Pressure Drop	129.89			129.92		
Particle Diameter						
(microns)	escaped	trapped	%trapped	escaped	trapped	%trapped
25	1079	329	23.4	850	257	23.2
50	569	841	59.6	475	619	56.6
75	340	1054	75.6	247	847	77.4
100	283	1109	79.7	134	960	87.8
125	162	1235	88.4	98	996	91.0
150	167	1248	88.2	92	1002	91.6
175	217	1198	84.7	125	969	88.6
200	268	1147	81.1	114	980	89.6
225	212	1203	85.0	202	892	81.5
250	265	1150	81.3	232	862	78.8

Separation Distance	8ft			9ft		
Pressure Drop	130.12			130.13		
Particle Diameter						
(microns)	escaped	trapped	%trapped	escaped	trapped	%trapped
25	663	418	38.7	583	86	12.9
50	229	853	78.8	520	149	22.3
75	111	971	89.7	247	414	62.6
100	178	904	83.5	51	618	92.4
125	183	899	83.1	15	652	97.8
150	119	963	89.0	13	656	98.1
175	128	954	88.2	23	646	96.6
200	116	966	89.3	55	614	91.8
225	159	923	85.3	69	600	89.7
250	191	891	82.3	112	557	83.3

Separation Distance	5ft			4ft		
Pressure Drop						
Particle Diameter						
(microns)	escaped	trapped	%trapped	escaped	trapped	%trapped
25	847	214	20.2	880	218	19.9
50	627	435	41.0	642	456	41.5
75	342	720	67.8	445	653	59.5
100	212	850	80.0	358	740	67.4
125	182	880	82.9	393	705	64.2
150	201	861	81.1	340	758	69.0
175	236	1400	85.6	347	751	68.4
200	226	836	78.7	344	754	68.7
225	292	770	72.5	351	747	68.0
250	316	746	70.2	342	756	68.9

APPENDIX D

Efficiency for Non-flanged Geometry with Varied Axial Gap

Axial Gap (in)	3			2		
Pressure Drop (Pa)	129.89			129.92		
Particle Diameter						
(microns)	escaped	trapped	%trapped	escaped	trapped	%trapped
25	744	460	38.2	1667	890	34.8
50	182	1026	84.9	431	2129	83.2
75	62	1145	94.9	162	2398	93.7
100	111	1097	90.8	136	2424	94.7
125	119	1089	90.1	153	2407	94.0
150	194	1014	83.9	275	2285	89.3
175	303	904	74.9	425	2135	83.4
200	392	816	67.5	586	1974	77.1
225	284	923	76.5	468	2092	81.7
250	376	831	68.8	574	1986	77.6

Axial Gap (in)	1			0		
Pressure Drop (Pa)	130.12			130.13		
Particle Diameter						
(microns)	escaped	trapped	%trapped	escaped	trapped	%trapped
25	2072	496	19.3	513	119	18.8
50	1161	1401	54.7	149	485	76.5
75	509	2075	80.3	57	577	91.0
100	157	2407	93.9	49	585	92.3
125	165	2402	93.6	44	590	93.1
150	181	2387	93.0	84	550	86.8
175	243	2325	90.5	120	514	81.1
200	380	2188	85.2	161	473	74.6
225	803	1756	68.6	132	502	79.2
250	862	1706	66.4	168	466	73.5

Axial Gap (in)	-0.5		
Pressure Drop (Pa)	130.19		
Particle Diameter			
(microns)	escaped	trapped	%trapped
25	449	183	29.0
50	192	436	69.4
75	71	561	88.8
100	45	587	92.9
125	78	554	87.7
150	105	527	83.4
175	171	461	72.9
200	213	419	66.3
225	182	150	45.2
250	220	412	65.2

APPENDIX E

Efficiency for Flanged Geometry with Varied Axial Gap

Axial Gap (in)	3			2		
Pressure Drop (Pa)	129.89			129.92		
Particle Diameter						
(microns)	escaped	trapped	%trapped	escaped	trapped	%trapped
25	877	374	29.9	621	473	43.2
50	794	458	36.6	476	618	56.5
75	790	462	36.9	400	694	63.4
100	509	743	59.3	168	926	84.6
125	297	955	76.3	104	990	90.5
150	194	1058	84.5	134	960	87.8
175	192	1060	84.7	223	871	79.6
200	223	1029	82.2	267	827	75.6
225	386	866	69.2	228	866	79.2
250	432	820	65.5	268	826	75.5

Axial Gap (in)	1			0		
Pressure Drop (Pa)	130.12			130.13		
Particle Diameter						
(microns)	escaped	trapped	%trapped	escaped	trapped	%trapped
25	2599	238	8.4	2215	305	12.1
50	2085	754	26.6	1475	1045	41.5
75	1526	1323	46.4	751	1769	70.2
100	827	2011	70.9	426	2092	83.1
125	381	2459	86.6	484	2036	80.8
150	433	2407	84.8	633	1887	74.9
175	509	2330	82.1	780	1740	69.0
200	613	2227	78.4	952	1568	62.2
225	1079	1761	62.0	821	1699	67.4
250	1211	1628	57.3	957	1563	62.0

Axial Gap (in)	-0.5				-1.5		
Pressure Drop (Pa)	130.19				130.16		
Particle Diameter							
(microns)	escaped	trapped	%trapped	escaped	trapped	%trapped	
25	805	117	12.7	709	170	19.3	
50	702	222	24.0	469	424	47.5	
75	588	336	36.4	349	544	60.9	
100	479	445	48.2	249	643	72.1	
125	345	579	62.7	188	705	78.9	
150	250	674	72.9	116	776	87.0	
175	260	664	71.9	159	734	82.2	
200	235	689	74.6	201	692	77.5	
225	337	587	63.5	334	558	62.6	
250	386	538	58.2	341	552	61.8	

APPENDIX F

Efficiency for varied CoR

CoR	1			0.8		
Particle Diameter						
(microns)	escaped	trapped	%trapped	escaped	trapped	%trapped
25	19062	3014	13.7	19000	3077	13.5
50	13403	8677	39.3	13065	9015	41.3
75	9028	13052	59.1	9299	12781	58.1
100	3022	19058	86.3	7737	14343	65.1
125	395	21685	98.2	4435	17645	79.2
150	390	21690	98.2	1689	20391	92.4
175	729	21351	96.7	900	21180	95.9
200	1222	20858	94.5	990	21090	95.5
225	1862	20218	91.6	1270	20810	94.2
250	2464	19616	88.8	1557	20523	92.9

CoR	0.6			0.4		
Particle Diameter						
(microns)	escaped	trapped	%trapped	escaped	trapped	%trapped
25	19000	3077	13.8	19000	3077	13.8
50	13065	9015	43.1	13065	9015	45.0
75	9299	12781	64.7	9299	12781	70.1
100	7737	14343	69.1	7737	14343	79.2
125	4435	17645	71.7	4435	17645	84.4
150	1689	20391	76.0	1689	20391	87.6
175	900	21180	81.0	900	21180	90.3
200	990	21090	84.6	990	21090	92.1
225	1270	20810	87.4	1270	20810	93.7
250	1557	20523	89.3	1557	20523	94.4

BIBLIOGRAPHY

- Akiyama, T., Marui, T., and Kono, M., (1986) Experimental investigation on dust collection efficiency of straight-through cyclones with air suction by means of secondary rotational air charge. *Industrial and Engineering Chemistry Process Design and Development* **25**, 914-918.
- Akiyama, T., and Marui, T., (1989) Dust collection efficiency of a straight-through cyclone – effects of duct length, guide vanes and nozzle angle for secondary rotational air flow. *Powder Technology* **58**, 181-185.
- Brock, J.D. (1997) Baghouse fines, Technical Paper T-121. Astec Industries, Chattanooga, TN.
- Chhabra, R.P., Agarwal, L., and Sinha, N.K. (1998) Drag on non-spherical particles: an evaluation of available methods. *Powder Technology* **101**, 288-295
- Fluent 6.0 Users Guide
- Gouesbet, G., Berlemont, A. (1999) Eulerian and Lagrangian approaches for predicting the behaviour of discrete particles in turbulent flows. *Progr. Energy Combust. Sci.* **25**, 133-159
- Griffith, W.D. and Boysan, F. (1996) Computational fluid dynamics (CFD) and empirical modeling of the performance of a number of cyclone samplers. *J. Aerosol Sci.* **27**, 281-304.
- Klujszo, L.A.C., Songfack, P.K., Rafaelof, M., and Rajamani, R.K. (1999) Design of a stationary guide vane swirl air cleaner. *Mineral Engineering* **12**, 1375-1392
- Lun, C.K.K. and Bent, A. A. (1994) Numerical simulation of inelastic frictional spheres in a simple shear flow. *J. Fluid Mech.* **258**, 335-353
- Ma, L. Ingham, D.B. and Wen, X. (1999) Numerical modeling of the fluid and particle penetration through small sampling cyclones. *J. Aerosol Sci.* **31**, 1097-1119
- Ramachandran, G., RRaynor, P.C. and Leith, D. (1994) Collection efficiency and pressure drop for a rotary-flow cyclone. *Filtration and Separation*, 631-636
- Swanson, M. (1999) Baghouse Applications, Astec Industries Technical Paper T-139. Chattanooga, TN.
- Vincent, R.A., (2001) Efficiency Analysis of the Cyclone Separator Using CFD Techniques, Masters Thesis, Georgia Institute of Technology, Atlanta, GA.

Xie, H. Y., and Zhang, D.W. (2000) Stokes shape factor and its application for measurement of sphericity of non-spherical particles. *Powder Technology* **114**, 102-105